In-Situ Infrared Spectroscopy Applied to the Study of the Electrocatalytic Reduction of CO_2
Theory, Practice and Challenges

Kas, Recep; Ayemoba, Onagie; Firet, Nienke J.; Middelkoop, Joost; Smith, Wilson A.; Cuesta, Angel

DOI
10.1002/cphc.201900533

Publication date
2019

Document Version
Accepted author manuscript

Published in
ChemPhysChem

Citation (APA)
Kas, R., Ayemoba, O., Firet, N. J., Middelkoop, J., Smith, W. A., & Cuesta, A. (2019). In-Situ Infrared Spectroscopy Applied to the Study of the Electrocatalytic Reduction of CO_2: Theory, Practice and Challenges. *ChemPhysChem*, *20*(22), 2904-2925. https://doi.org/10.1002/cphc.201900533

In-situ infrared spectroscopy applied to the study of the electrocatalytic reduction of CO_2: Theory, practice and challenges

Recep Kas,[a] Onagie Ayemoba,[b], Nienke J. Firet[a], Joost Middelkoop[a], Wilson A. Smith*[a] and Angel Cuesta*[b]

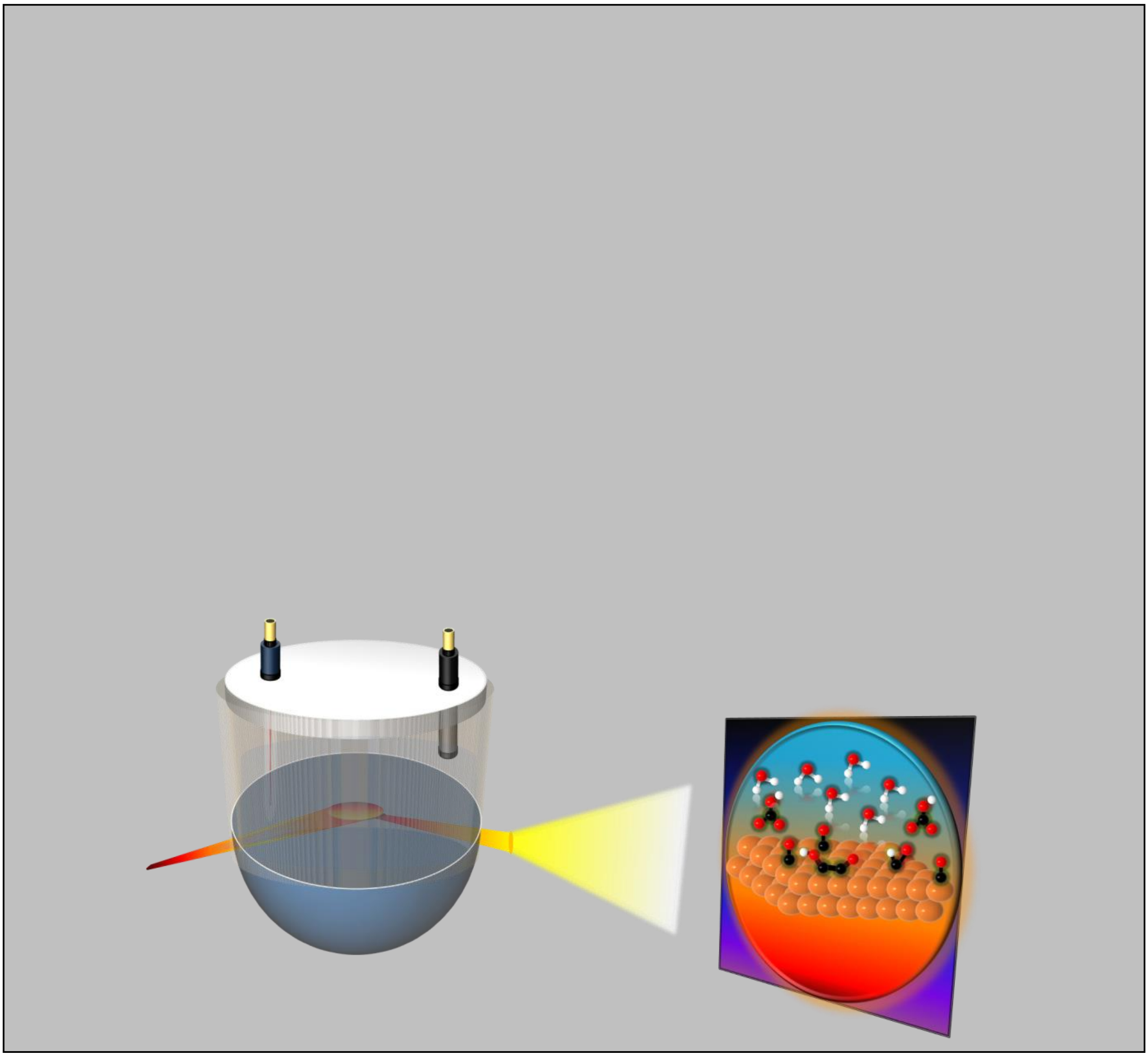

Abstract: The field of electrochemical CO_2 conversion is undergoing significant growth in terms of the number of publications and worldwide research groups involved. Despite improvements of the catalytic performance, the complex reaction mechanisms and solution chemistry of CO_2 has resulted in a considerable amount of discrepancies between theoretical and experimental studies. A clear identification of the reaction mechanism and the catalytic sites are of key importance in order to allow for a qualitative breakthrough and, from an experimental perspective, calls for the use of *in-situ* or *operando* spectroscopic techniques. *In-situ* infrared spectroscopy can provide information on the nature of intermediate species and products in real time and, in some cases, with relatively high time resolution. In this contribution, we review key theoretical aspects of infrared reflection spectroscopy, followed by considerations of practical implementation. Finally, recent applications to the electrocatalytic reduction of CO_2 are reviewed, including challenges associated with the detection of reaction intermediates.

1. Introduction

Reducing carbon dioxide (CO_2) emissions while simultaneously sustaining global economic growth is one of the most important global challenges.[1] Because of the scale of the problem, a range of different technical approaches will be needed to reduce CO_2 emissions and associated negative effects, and different technologies might be more appropriate in different scenarios, depending on industry, location and other constraints.[2] Currently, renewable fuels are produced predominantly from biomass, which involves the use of crops and land that might be needed to feed the planet's increasing population. The electrochemical reduction of CO_2 has the potential to enable industrial scale production of fuels by storing renewable electricity in chemical bonds.[3]

Intensive research on the electrochemical reduction of CO_2 was pioneered by Hori in the 1980s,[4–6] although early reports date from as far back as 1954[7] and some more work was done during the 1970's.[8–14] The electrocatalytic reduction of CO_2 has been shown to result in a variety of products including CO, formic acid, alcohols, and hydrocarbons. Almost a decade ago, Hori provided an excellent review of global scientific work during the first decade of this century, focused on activity and selectivity trends.[15] A recent review of work with single-crystal metal electrodes was also recently published.[16] From these reviews, it is apparent that nearly all metals suffer from high overpotentials and low stability, while some metals including Ag, Au, Pb and In have reasonable selectivity towards 2 electron transfer products (CO and formic acid/formate).[17–20] Significant progress has been made in understanding the underlying mechanisms behind the activity and selectivity of CO_2-reduction electrocatalysts during the last 5 years,[21,22] as the number of people working in the field (and consequently the number of publications) has increased significantly. In addition, substantial improvements have been achieved in the selectivity and activity of electrocatalysts with the use of nanostructured electrodes along with density functional theory (DFT) calculations.[23,24] However, significant improvements are still needed on the activity and stability of catalysts to meet commercial expectations and compete with the current production methods based on fossil fuels.[17,25,26]

Understanding the nature of relevant intermediates and their interaction with a catalyst surface not only allows optimization of existing catalysts, but also provides important information to aid in the rational design of new catalysts. In-situ spectroscopy studies in catalysis allow testing and refining of proposed mechanisms by providing crucial information on the structure and binding of the reaction intermediates in operando conditions. Infrared spectroscopy is one of the classical techniques used in catalysis for in-situ monitoring the interaction between molecules in a solution and a catalyst surface.[27] Due to its sensitivity towards chemical composition and chemical environment in both gaseous and condensed phases, this technique has been commonly used in heterogeneous catalysis since the 1950s.[28,29] The first applications to the electrode/electrolyte interface date from 1970, and made use of the attenuated total reflection (ATR) geometry with infrared-transparent semiconductor electrodes.[30] Breakthroughs were achieved by Bewick and co-workers in 1980,[31] with the first external-reflectance (also called infrared reflection-absorption spectroscopy, IRAS) spectra at the metal-electrolyte interface, and during the 1990's by Osawa and co-workers,[32–35] who, by depositing thin metal films on infrared-transparent substrates, managed to combine the ATR geometry and the phenomenon of surface-enhancement of the infrared absorption (SEIRA). Although IRAS allows the use of single-crystal electrodes, thereby enabling studies of structure activity relationships, SEIRA spectroscopy in the attenuated total reflection configuration (ATR-SEIRAS), has a sensitivity 1-2 orders of magnitude higher and is not limited by the high electrical and transport resistances typical of the thin-layer configuration necessary for IRAS, leading to improved time resolution and allowing for experiments in *operando* conditions. Infrared spectroscopy has become an indispensable tool in electrochemistry, and particularly in electrocatalysis, since it allows in-situ, non-destructive and label-free analysis of species at the electrode-electrolyte interface.[36] Recently, there has been a growing interest in the application of in-situ infrared spectroscopy to track the reaction intermediates and understanding the kinetics and mechanism of the electrochemical reduction of CO_2.[37] The aim of this review is to summarize theoretical and experimental aspects of these spectroscopic techniques, and to describe the challenges and possibilities of the application of infrared spectroscopy to understanding the electrocatalytic reduction of CO_2. Section 2 summarizes the theory of reflection spectroscopy in the two possible geometries, the SEIRA effect and band shapes. Section 3 discusses crucial details of experimental design. Finally, Section 4 provides an overview of the recent literature to illustrate potential usage and limitations of these techniques for future electrochemical applications.

---

[a] Dr. R. Kas, Nienke Firet, Joost Middelkoop, Prof. W. Smith
Department of Chemical Engineering
Delft University of Technology
2629 HZ Delft, The Netherlands
E-mail: w.smith@tudelft.nl
[b] O. Ayemoba, Prof. A. Cuesta
School of Natural and Computing Sciences
University of Aberdeen
Aberdeen AB24 3UE, Scotland, UK
E-mail: angel.cuestaciscar@abdn.ac.uk

Recep Kas obtained his B.Sc. in Chemistry and M.Sc. in Materials Science from Koc University in 2009 and 2012 respectively where he worked on various type of inorganic nanoparticle synthesis . He completed his phd in 2016 in University of Twente on electrochemical CO_2 reduction before beginning his postdoctoral work at Delft University of Technology. His interests are understanding kinetics and mechanism of electrochemical reactions by combining electrochemistry with in-situ spectroscopy and online analytic techniques and development of new electrocatalysts by using chemical and physical depositon techniques.

Onagie Ayemoba obtained her B.Sc. in Chemistry from Madonna University (Nigeria) in 2014 and an M.Sc. in Oil and Gas Chemistry from the University of Aberdeen in 2015. She is currently working towards a Ph.D. in the department of chemistry at the University of Aberdeen (Scotland, UK). Her doctoral research is focused on the fundamental study of interfacial electrochemical processes which includes CO_2 electroreduction using ATR-SEIRAS.

Nienke J. Firet works as a PhD researcher in the Department of Chemical Engineering at Delft University of Technology. Her research focusses on operando methods such as infrared and X-ray absorption spectroscopy to study electrochemical CO_2 reduction. She obtained two masters: Chemical Engineering and Sustainable Energy Technologies from the University of Twente in 2015. Before this she received a Bachelor's degree from Delft University of Technology in Molecular Science and Technology.

Joost Middelkoop works as a Research Technician in the Department of Chemical Engineering at Delft University of Technology. With a strong focus on equipment design. He obtained his Bachelor degree in Mechanical Engineering from the Fontys Hogeschool Eindhoven in 2003.

Wilson A. Smith is an Associate Professor in the Department of Chemical Engineering at Delft University of Technology. He earned his BS in Physics from American University in 2005, and his PhD in Physics from the University of Georgia in 2010, where he studied the synthesis and applications of nanostructured photocatalysts. From there he moved to Paris, France as a postdoctoral research associate at the Universite Pierre et Marie Curie/Sorbonne where he studied the defect structure of doped semiconductors for solar water purification. In 2012 he began his independent career at TU Delft, where his group focuses on fundamental and applied aspects of photoelectrochemical water splitting, electrochemical CO2 reduction and ammonia synthesis. Wilson has been the recipient of the prestigious VENI (2013), VIDI (2016), and ERC Starting (2017) personal grants, which have helped his group bridge scales and disciplines to address practical problems in large scale energy conversion and storage.

Angel Cuesta graduated in Chemistry from the University of Zaragoza (Spain) in 1992 and obtained his PhD in 1996 from the Autonomous University of Madrid (Spain) for a thesis developed at the Institute of Physical Chemistry "Rocasolano" (CSIC, Madrid) under the supervision of Prof. C. Gutiérrez. After a postdoctoral period with Prof. D. M. Kolb (University of Ulm, Germany) he became a Staff Scientist of the Institute of Physical Chemistry "Rocasolano" in 2001. Since 2018 he is a full professor at the University of Aberdeen (Scotland, UK). His research interests include fundamental aspects of interfacial electron transfer, structure of the electrical double layer and electrocatalysis.

2. Fundamental aspects of infrared spectroscopy at electrode–electrolyte interfaces

The energy of mid-infrared (mid-IR) radiation matches the separation between the energy levels of unique vibrational modes in molecules, offering fingerprint spectra. Functional groups, molecular symmetry, as well as both intramolecular and intermolecular interactions can be monitored with infrared spectroscopy, which can be used to obtain information regarding the geometry and orientation of molecules adsorbed on catalytic surfaces.[38] Infrared spectroscopy had been used for decades in gas phase heterogeneous catalysis before first being applied to the study of electrochemical reactions in aqueous electrolytes, which is much more challenging due to the intense infrared absorption of water. Although non-aqueous solvents are usually less strong infrared absorbers than water, absorption by either the solvent or the electrolyte ions is still an issue to be taken into account, particularly in the case of ionic liquids, an electrolyte medium with increasing popularity. In order to minimize the path length of infrared light through the electrolyte, thereby minimising absorption by its components, two different approaches have been adopted. Specular (or external) reflection and internal reflection of light (Fig.1), lead to IRAS and ATR configurations, respectively. It is worth noting that all metals have a very high reflectivity in the IR region, and their contribution to the (differential) IR reflectance spectra is minimal, and consists at most of a featureless, potential-dependent baseline. However, if the reflectivity of the electrode surface is low, the band shape of vibrational modes of adsorbed species can be affected, and the optical properties of the substrate must also be taken into account when interpreting the spectra.[39]

2.1. Infrared Reflection Absorption Spectroscopy (IRAS)

In the external reflection configuration, commonly known as IRAS, the metal electrode is pressed against an infrared-transparent window forming a thin electrolyte layer (1-10µm) between the window and the electrode (Fig. 1a). The beam passes through the optical window and crosses a very thin layer of electrolyte solution before it is reflected from the electrode surface.

In order to maximize the signal-to-noise ratio and the sensitivity to adsorbed species, both the polarisation state of the infrared radiation and the angle of incidence at the electrode-electrolyte interface must be chosen adequately. A schematic representation of the external reflection of light from metal surfaces is given in Fig. 2a. The electric field of both the incident and reflected beams can be decomposed into *s*- and *p*-polarized light, with the electric field of the radiation oscillating perpendicular and parallel, respectively, to the plane of incidence. Due to the high reflectivity of metals in the infrared region, the *s*-polarized component suffers a phase shift of 180° upon reflection at all angles of incidence. This results in the destructive interference of the electric fields of the incident and reflected beams, E_s^{i} and E_s^{r}, respectively, at the interface.[40] The resulting null intensity of the *s*-polarized electric field at the interface (Fig. 2c) makes interaction with adsorbed molecules impossible, and using *s*-polarised light will result in spectra containing information exclusively about species dissolved in the thin layer of electrolyte trapped between the electrode and the infrared-transparent window.

The *p*-polarized component of the radiation can be further decomposed into two components, one parallel and one perpendicular to the interface ($E_{p\parallel}$ and $E_{p\perp}$, respectively). As in the case of *s*-polarised light, the incident and reflected beams of $E_{p\parallel}$ ($E_{p\parallel}^{\mathrm{i}}$ and $E_{p\parallel}^{\mathrm{r}}$, respectively) are out of phase at all angles of incidence and cannot interact with adsorbates. On the other hand, the phase difference between the incident and reflected beams of $E_{p\perp}$ ($E_{p\perp}^{\mathrm{i}}$ and $E_{p\perp}^{r}$, respectively) is negligibly small up to a high angle of incidence, changing rapidly to 180° when approaching grazing incidence. $E_{p\perp}^{\mathrm{i}}$ and $E_{p\perp}^{\mathrm{r}}$ increase with increasing angle of incidence (at grazing incidence $E_{p\perp} \approx E_p$ and $E_{p\parallel} \approx 0$). Therefore, the amplitude of the oscillating electric field perpendicular to the surface at the interface (which results from the constructive interference of $E_{p\perp}^{\mathrm{i}}$ and $E_{p\perp}^{\mathrm{r}}$) reaches a broad maximum at high angles of incidence (Fig. 2c and 2d).[40,41] The calculated angle of incidence at which $E_{p\perp}$ is maximum ranges between 80° and 89°, depending on the metal and the infrared frequency. However, the angular divergence of the infrared beam results in a spread of the incident angle of ±6°, which shifts this angle to values between 75° and 80°.[39]

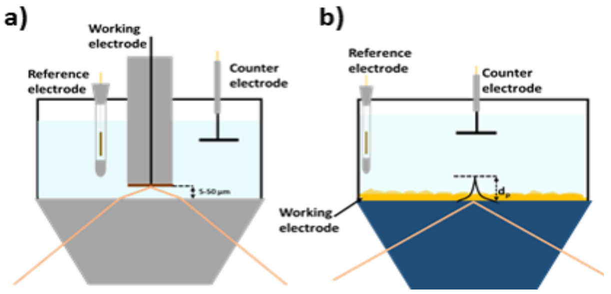

Figure 1: The two most commonly used geometries for infrared experiments at the electrode-electrolyte interface. a) External reflection b) Internal reflection

The consequences of the fundamental mechanisms of light polarization described above are multifold:

1. Since the intensity of infrared absorption is directly proportional to the product between the intensity of the electric field of the radiation and the dynamic dipole moment of the vibrational mode, an angle of incidence at the electrode-electrolyte interface as close as possible to that at which $E_{p\perp}$ at the interface is maximum must be chosen. This will be discussed in more depth later in the section devoted to experimental details.
2. Since the intensity of the electric field of *s*-polarised light is negligible at the interface, only *p*-polarised light carries information from the species present at the electrode surface. If interested in adsorbates, improved signal-to-noise ratio can therefore be achieved by using *p*-polarised instead of unpolarised radiation. This also allows for easy distinction between adsorbed species and species in solution, as the latter will appear both when using *p*- and *s*-polarised light, while the former will only appear if *p*-polarised radiation is used.
3. Since only the component of the *p*-polarised radiation perpendicular to the interface has a finite intensity of
4. the electric field at the interface, only vibrational modes with a component perpendicular to the surface can interact with the infrared radiation, and IRAS is blind to vibrational modes parallel to the surface. This is usually known as the surface selection rule.
5. Since the intensity of an oscillating electric field scales with the square of the oscillation amplitude (*i.e.*, the intensity of absorption is not proportional to $E_{p\perp}$, but to $|E_{p\perp}|^2$), at the optimal angle of incidence the effective absorption cross-section of a vibrational mode perfectly perpendicular to the surface is more than twice (see Fig. 2(c)) that of the same vibrational mode in transmission (assuming that the dynamic dipole moment and the Einstein absorption coefficient of the vibrational mode do not change upon adsorption).

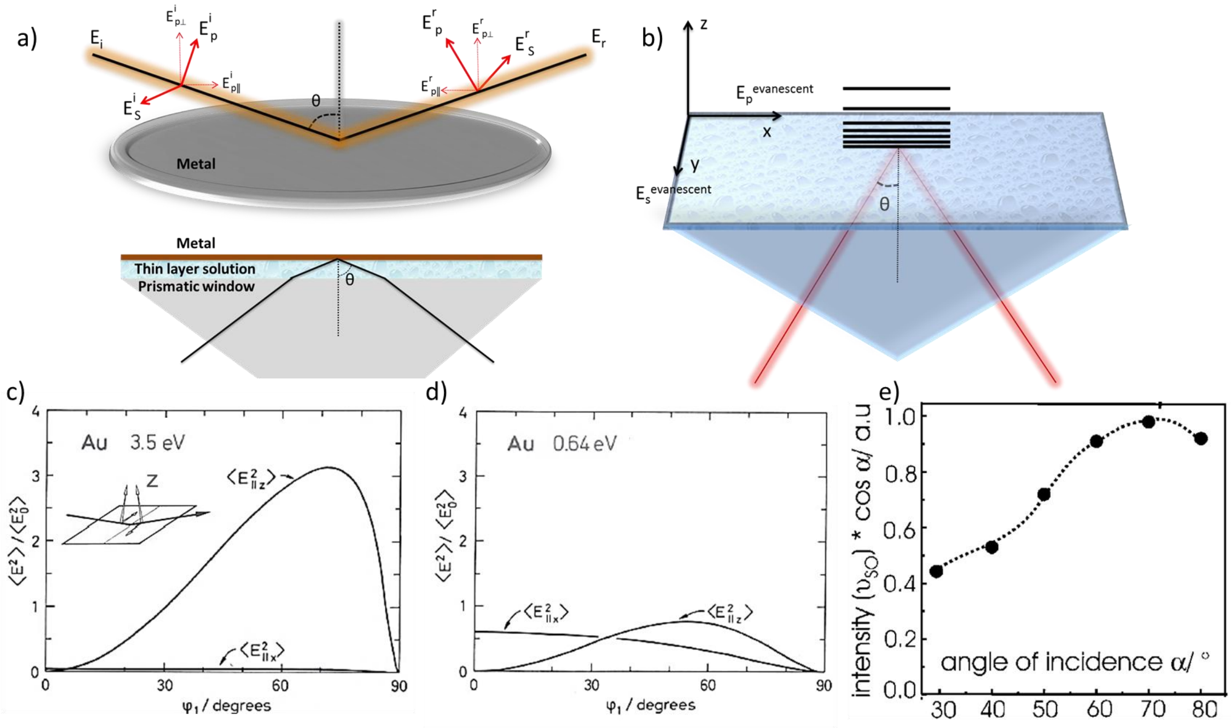

Figure 2: Schematics of s and p components incident beam and reflected radiation for different geometries: IRAS (a) and ATR (b); Dependence of the intensity of the electric field at the interface on the angle of incidence for a highly reflecting (c) and a moderately reflecting (d) surface (From [40]); e) dependence of the intensity of the absorbance of the on the angle of incidence in ATR-SEIRAS for the υ_{SO} mode of sulphate specifically adsorbed on a thin-film gold electrode deposited on Si (From ?).

The major advantage of IRAS is that it allows measurements with a wider range of electrode materials, including single crystal electrodes. However, the thin layer configuration severely restricts mass transport to and from the interface, precluding *operando* experiments. The thin layer configuration also results in a large uncompensated resistance, which leads to a very large cell time constant, severely decreasing the time resolution achievable. When large currents flow, the large uncompensated resistance will result in a non-negligible difference between the actual electrode potential and the applied potential, which will increase with increasing current. Finally, in the particular case of CO_2 electroreduction, which in aqueous solutions is nearly always accompanied by hydrogen evolution, bubbles trapped in the thin layer will generate large solvent bands due to the displacement of the electrolyte form the optical path, eventually masking bands due to products or intermediates. This problem will be less severe when working in non-aqueous solvents or in ionic liquids, where hydrogen evolution is strongly inhibited, but otherwise might render this geometry of little, if any, use for studying the electrocatalytic reduction of CO_2.

2.2. Attenuated Total Reflection (ATR)

Some of the problems associated with IRAS can be addressed by using ATR in the Kretschmann configuration, in which a thin metal film is deposited onto an infrared-transparent material with a high refractive index, and used as the working electrode (Fig. 1b). ATR makes use of the phenomenon of internal reflection, which happens when an incident beam travelling through a transparent material with a high refraction index, n_1, (known as the internal reflection element, IRE) reaches the interface between the IRE and a medium with a lower refraction index, n_2, at an angle of incidence, ϑ_i, larger than the critical angle, $\theta_\mathrm{c} = \sin^{-1}(n_2/n_1)$. Under these conditions ($\vartheta_\mathrm{i} > \theta_\mathrm{c}$), the beam is totally reflected at the interface, and no radiation is transmitted from the IRE into the other medium. As in the case of IRAS, interference between the incident and reflected beam also generates a standing wave at the interface, although, because now none of the two media have a high reflectance, both the parallel and perpendicular components of the electric field of this standing wave are finite and of similar magnitude.

The electric field of this standing wave penetrates the medium above the IRE, forming an evanescent field (the so-called *evanescent wave*) whose intensity decreases exponentially with increasing distance from the interface according to Equation 1:

$$I = I_0 \exp\left(\frac{-z}{d_\mathrm{p}}\right) \qquad (1)$$

Where I_0 is the intensity of the electric field at the interface, z is the distance to the interface, and d_p is the penetration depth, at which $I = I_0/e$ (*i.e.*, d_p roughly corresponds to the thickness of electrolyte that can be probed by the evanescent wave). For total reflection at the interface between a transparent window and an electrolyte, d_p depends on the wavelength (λ) the refraction indexes of the IRE (n_1) and the electrolyte (n_2) and the incidence angle (θ), as described by Equation 2:

$$d_{\mathrm{p}} = \frac{\lambda}{2\pi n_1 \sqrt{\sin^2\theta_{\mathrm{i}} - (n_2/n_1)^2}} \qquad (2)$$

The deposition of a thin metal film on the surface of the infrared-transparent material will obviously change the optical properties of the interface, and an exact quantitative treatment of the problem would require the use of a three-layer model and of effective medium theory to calculate an effective refraction index (n_{eff}) for the thin layer between the infrared window and the electrolyte, which will not be discussed in detail here. Briefly, the value of n_{eff} will be determined by the fill factor, f, that is, the fraction of the volume of the thin film that is occupied by metal particles. In general, for sufficiently thin metal films, using $n_2 \approx n_{\mathrm{eff}}$ allows for a good approximation of d_{p}.[42,43] For very high fill factors (*i.e.*, very thick metal films), the geometry is not that of internal reflection any more, but instead that of external reflection (like in IRAS), with no possibility of probing the metal-electrolyte interface due to the very high reflectivity of metals in the infrared. Therefore, probing (metal) electrode-electrolyte interfaces requires films conductive enough to do electrochemistry but at the same time thin enough to allow the evanescent wave to reach the electrode/electrolyte interface.

Interaction of the evanescent wave with vibrational modes within its penetration depth will provoke a decrease in the intensity of light reaching the detector at the corresponding frequency (i.e., an attenuation of the totally reflected beam), hence the term ATR. For typically used IRE materials like Si or Ge and aqueous electrolytes, at an angle of incidence of 60°, d_{p} varies roughly between 150 and 700 nm between 4000 and 1000 cm^{-1}, respectively, (please note that d_{p} will show large variations around 3500 and 1645 cm^{-1}, where the refraction index of water shows considerable oscillations due to excitation of the $\tilde{\upsilon}_{\text{O-H}}$ and $\delta_{\text{H–O–H}}$ modes of water). Thin metals films are strong infrared absorbers and/or reflectors depending on thickness and morphology, and deposition of even a thin metallic film might be enough to damp the intensity of the evanescent wave beyond the expected exponential decay. For example, in the case of copper at 2000 cm^{-1}, a thickness of just 50 nm will be sufficient to decrease the intensity of the evanescent wave to I_{o}/e.[44] Therefore, for electrochemical ATR experiments the thickness of the metal films on the IRE are kept typically below 100 nm. The thickness of the electrolyte layer probed will strongly depend on the actual thickness and morphology of the metal film, and will vary typically from several nm to tens of nm. This makes the ATR configuration particularly well suited for the *in-situ* detection of adsorbates at electrode surfaces with minimum interference from the bulk electrolyte[39] However, any species present within the probed distance in sufficiently high concentration and/or with a large enough absorption coefficient can be detected. For example, formic acid in the electrolyte above the electrode can be detected using ATR-SEIRAS at concentrations well below 0.1 M,[45–47] and ATR-SEIRAS has been used to determine the local pH during the electroreduction of CO_2 at the electrode-electrolyte interface by probing the ratio between the concentrations of CO_2 and HCO_3^- in the electrolyte just above the electrode.[48]

2.3. The SEIRA effect: ATR-SEIRAS

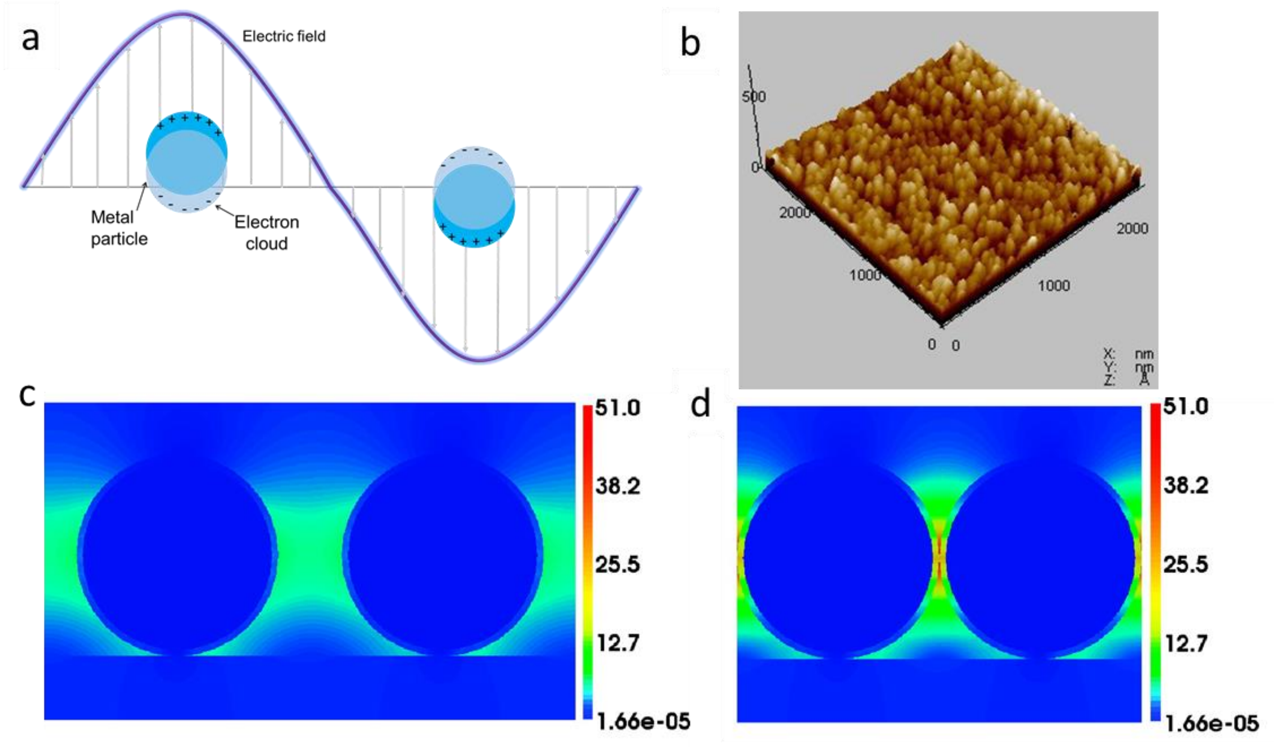

Figure 3: a) illustration of the excitation of localized surface plasmon resonance. b) AFM image of gold nanoparticle film deposited on Si. c) and d) Simulation of the electromagnetic field strength around a nanoparticle for 30 nm coated gold nanoparticles and interparticle spacing of 10 nm (c) and 0 nm (d).

Absorption of infrared radiation by a vibrational mode is proportional to the product between the square of the amplitude of the electric field and the vibrational mode's dynamic dipole moment. Therefore, it is possible to enhance IR absorption by increasing the electric field felt by the absorbing molecules. As mentioned previously in Section 2.1, the larger amplitude of the electric field perpendicular to the electrode surface leads to an increased absorption by adequately oriented vibrational modes in IRAS, as compared with absorption by the same vibrational mode in transmission. However, because ATR requires reflection at the surface of a transparent medium, no enhancement of the amplitude of the electric field of the standing wave occurs for either the *p*- or the *s*-polarised components of the radiation. Fortunately, ATR can be combined with the SEIRA effect, although it is important to emphasize here that SEIRA is not exclusive of the ATR configuration, and can also be observed in transmission and in IRAS.

In SEIRAS, enhancement factors of up to 100 be achieved,[35] enough to enable detection of sub-monolayer adsorbates and intermediates on metal surfaces under operando conditions.[49]

The exact mechanism of the enhancement effect of SEIRA has been amply discussed in the literature[50,51] and, like the similar phenomenon of the surface enhancement of Raman scattering (SERS), is attributed to two different contributions, namely, electromagnetic and chemical origins.[32] However, we would like to note that unlike in SERS, which, with just some exceptions,[52] is limited to the coinage metals, SEIRAS seems to be much less substrate-specific, and reasonable enhancement has been reported from iron,[53,54] platinum,[55,56] palladium[57–60] and silicon carbide[61] particles.

The electromagnetic mechanism of SEIRA emerges from the excitation of localized surface plasmons.[35,51,62–64] Plasmons are longitudinal waves formed by the collective oscillation of electrons in metals, which can interact with light to give rise to absorption, scattering and/or re-emission of the incident photons from the metal surface, depending on the plasma frequency. The high reflectance of metals in the visible and, particularly, the IR spectral region is a result of their high plasma frequency. Below the plasma frequency, collectively oscillating electrons relax by emitting photons of a frequency identical to that of the radiation that generated the oscillation, without any energy dissipation. At the plasma frequency, energy is absorbed and dissipated due to plasmon resonance (this being, for example, the reason for the yellow and red colors of gold and copper, respectively). Above the plasma frequency, metals are transparent.

Plasmons can be confined at the interface between a metal and a dielectric, in which case they are called surface plasmon polaritons (SPP) or, simply, surface plasmons.[65] Surface plasmons can be excited by photons, but this requires the presence of an oscillating electric field parallel to the interface, which is impossible for reflection of an infrared beam from a highly reflecting flat metal surface. Coupling between photons and SPPs, can be achieved, though, using ATR, either in the Kretschmann or the Otto configuration, thanks to the electric field parallel to the interface sustained at the surface of the IRE. SPPs can also be excited in external reflectance if the metal surface is very rough and has a low reflectance (as in the case of a very finely divided metal deposit consisting of small enough particles like, *e.g.*, platinum black),[42,43] or in transmission, by depositing an ultrathin metal film on, or embedding metal particles in, an infrared transparent support.

In the case of nanoparticles with sizes comparable to or smaller than the radiation wavelength, surface plasmons cannot propagate and remain confined within the particle. The polarization of the metal particle resulting from the collective oscillation of the electrons tends to be restored by the positively charged nuclei left behind, as schematically depicted in Fig. 3(a).[66] There is a frequency at which these two effects are in resonance, known as the localized surface plasmon resonance (LSPR), at which the localized surface plasmon can be excited. Excitation of a localized surface plasmon generates an electric field around the particles which is stronger than the incident field of the photons, and which falls off quickly with distance from the particle surface.[67] This can be viewed as an intensification of the photon flux and a confinement of the optical field in the vicinity of the metal nanostructures. When molecules are located inside this near-field, absorption by their vibrational modes is enhanced.

For metals, the LSPR usually lies in the visible and near-IR part of the spectrum, unless they are carefully engineered.[68] However, the LSPR is very sensitive to changes in the refraction index of the surrounding medium, which can be provoked, among other things, by the proximity of other particles. SEIRA-active films are usually composed of randomly grown continuous interacting metal islands or nanostructures grown on, or embedded in, an infrared transparent material (see, e.g., the atomic force microscope (AFM) image of a typical SEIRA-active gold film deposited on Si, composed of densely packed Au islands with a diameter of 50 nm, shown in Fig 3(b)[69]. The close proximity between particles in the film broadens the LSPR and shifts it to higher wavelengths.[32,70–72] The tail of the absorption band extends into the mid-IR region, and this is considered to be sufficient to explain the major source of SEIRA.

The local electric field around metal nanostructures under electromagnetic irradiation can be calculated by using Maxwell's equations for the static limit[66,73] (since metal nanostructures are much smaller than the wavelength of the mid-IR radiation, they can be assumed to be under a constant electric field). This is often done by using an effective medium theory (EMT) to determine an effective complex dielectric constant for the metal film, which can be considered as a composite of the metal particles, eventually covered by an IR-absorbing adsorbate, and a dielectric medium (the electrolyte in electrochemical systems). EMTs have been used extensively in the past to calculate electromagnetic SEIRA enhancement factors and band shapes for metal nanostructures coated with an adsorbate.[32,35,42,43,74] Maxwell-Garnett's EMT is one of the most used, and is successful in predicting band shape, although problems predicting the enhancement factors are often encountered near the percolation limit, due to the assumed weak interactions between the metal nanostructures.[63,75,76] On the other hand, Bruggeman's EMT is good at predicting enhancement factors when the metal nanostructures are densely packed and there is considerable difference in the permittivity of the metal and the adsorbate.[35,42,43,55,77] An extensive discussion on the application of EMTs to SEIRA can be found in the detailed review by Griffith et al.[50] More advanced methods include taking into account the finite number of particles strongly interacting in a well-defined way, *i.e.*, finite element method (FEM) and finite difference time domain method, which can directly simulate the local electric field distribution around the metal nanostructures. However due to the complexity of these calculations for complex geometries, they were introduced much later than EMT models for SEIRA after recent advances in numerical methods to solve Maxwell's equations.[64,71] The local electric field distribution around 30 nm gold nanoparticles with a 1 nm thick polyethylene coating is shown in Fig 3(c) and 3(d), as calculated using FEM.[69] Regardless of the method used to calculate the electromagnetic contribution to the enhancement a sharp decay of the effect with distance, and a confinement of SEIRA to molecules within 5-10 nm of the surface were predicted,[78] due to the quadratic dependence of the intensity of the IR absorbance on the local electric field.

It has been firmly established that the degree of enhancement is dramatically influenced by the distance between the metal particles.[35,62,69,79] For instance, Fig. 3c and 3d show simulations of the electric field strength between two gold particles separated by 10 nm and 0 nm, respectively.[64] The strength of the electric field is at least one order of magnitude larger around the contact point of the particles when compared to spheres with larger separation. This is attributed to the interparticle plasmon coupling of the nanostructures, which is much stronger than the coupling with the surrounding medium.[72] Noticeable enhancements are found to start when $d \leq 2R$, where d is the center to center distance between nanostructures and R is the particle radius, and increases as the gap between nanostructures shrinks.[80] This is in line with experimental data, since the maximum enhancements are usually observed when the nanostructures are closely packed but are not completely merged together.[79,81,82]

Another electromagnetic contribution often overlooked in SEIRA is the 'lightning rod' effect, which is the result of higher charge density at the sharper tips of non-spherical nanostructures.[83,84] The consequence of this effect is that electric fields, and therefore the enhancement of absorption, is particularly intense from the points with large curvature, such as the tip of prolate ellipsoids, nanoneedles, etc.[73,85]

Infrared absorption of the molecules at the vicinity of metals can be further enhanced by shifting the surface plasmon resonance to the mid-IR region via carefully engineering the size and shape of the nanostructures.[86] Enhancement factors up to 10^5 have been reported in the vicinity of individual and coupled nanorods and nanowires, which are commonly referred to as nanoantennas.[87–90] However, the application of nanoantennas to the study of electrode-electrolyte interfaces has, to the best of our knowledge, not been reported yet. Possible application of these structures to the study of electrocatalytic reactions will be discussed in the final section of this review.

In addition to the electromagnetic mechanism of SEIRA discussed above, Osawa and co-workers identified an additional chemical mechanism that exists on very thin (< 5 nm) metal films, for which the absorption band of surface plasmons does not extend to the mid-IR region.[32,35] The chemical enhancement is considered to occur due to the charge transfer between the molecule and fermi level of the metals, which changes in charge distribution, and thus the dipole moment of the adsorbed molecules.[91,92] Alternative explanations for chemical mechanisms are based on the photoinduced charge transfer between the metal and adsorbed molecules.[63] When the energy of the incident photons is equal to the energy gap of electron transfer between the metal and adsorbed molecules, a resonance is formed which increases the dynamic dipole moment of the vibrational mode and, hence, the infrared signal.[93]

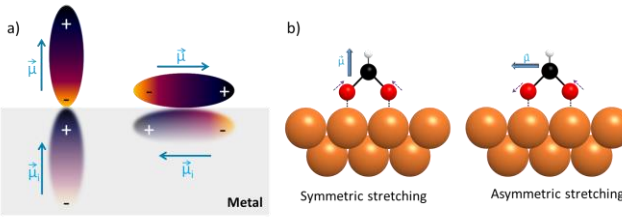

Figure 4: a) Image dipole changes in the same direction with a vibration of dipole normal to the surface and changes in the opposite direction with a vibration of dipole parallel to the surface. b) Symmetric and asymmetric stretching of adsorbed formate molecule create dipoles perpendicular and parallel to the surface, respectively.

Studies from various researchers suggested that the chemical effect can be much more prominent in some cases compared to the plasmonic effects, especially for strongly polarizable functional groups.[50,94] Experimental and theoretical studies suggest that the electronic and geometric structure of adsorbed molecules, the surface structure of the metal and the bonding between the molecules and metal play a crucial role on the magnitude of chemical enhancement. In general, both the electromagnetic and the chemical mechanisms will contribute to SEIRA, the degree of contribution of each mechanism varying depending on the type of metal and adsorbed molecule.

In ATR-SEIRAS the properties of ATR are coupled to those of SEIRAS. The main advantages of ATR-SEIRAS over IRAS are (i) the increased sensitivity to adsorbed species, (ii) the significantly lower interference from the bulk of the electrolyte and (iii) the significantly decreased IR drop and transport limitations. The high sensitivity to adsorbed species often allows spectral collection with good signal-to-noise ratio with a single interferogram, which coupled to a faster response due the much lower electrolyte uncompensated resistance allows for a considerably improved time resolution. The much-improved transport conditions allow for experiments under operando conditions. With well-designed flow cells, experiments under controlled transport conditions can be performed.[95]

As in IRAS, the surface selection rule also applies in ATR-SEIRAS. However, unlike in IRAS, where only *p*-polarized light carries information from the electrode surface, in ATR-SEIRAS the intensity of the infrared electric field parallel to the surface is not zero, which is in fact necessary in order to generate the LSPR responsible for the electromagnetic contribution to the SEIRA effect. A consequence of this is that, while in IRAS, improved signal-to-noise ratio of adsorbate bands is achieved when using *p*-polarized radiation, while in ATR-SEIRAS the use of non-polarized light is preferable.

It could be expected that due to the non-zero intensity of the IR electric field parallel to the interface, vibrational modes perfectly parallel to the electrode surface would also be active in ATR-SEIRAS. However, electric fields on the surface of a conducting material are always perpendicular to the surface at every point regardless of the surface structure[96] (*i.e.*, including at the surface of a metal particle) and, therefore, interaction is, also in ATR-SEIRAS, only possible with vibrational modes perpendicular to the surface.[63]

An alternative, and equivalent, explanation is illustrated in Fig. 4(a): the molecular dipole associated to a vibrational mode of an adsorbed molecule induces an image dipole in the metal surface, where the interaction between two dipoles depends on the molecular orientation with respect to the surface. The dipole change is completely cancelled out by the image dipole when the vibrational mode is parallel to the surface. In contrast, dipoles oscillating perpendicular to the surface will be reinforced by the image dipole.[41,97] The result is that only vibrational modes with a dipole change perpendicular to the surface will be active.[78] An example of the surface selection rule is given in Fig. 4(b), showing a model of formate adsorbed onto metal surface in a bridging configuration, *i.e.*, bonded through the oxygen atoms to two surface copper atoms. Both the symmetric and asymmetric stretching modes of formate are IR active, and appear around 1380 and 1580 cm^{-1} in a transmission spectrum. Since the dipole moment change of the asymmetric stretching is parallel to the surface, only the symmetric stretching mode of the formate will be active, both in SEIRAS and IRAS.[56]

2.4. The shape and intensity of adsorbate bands

Due to the differential nature of both IRAS and ATR, adsorbates can generate both negative and positive absorbance bands, as well as bipolar bands. This, however, is due to the acquisition method and does not reflect the intrinsic shape of the bands, which will be discussed explicitly in this section.

Two main factors affect the shape and intensity of adsorbate bands. One is the interaction between oscillating adsorbed dipoles when in close proximity (dipole-dipole coupling), and the other is the presence of dispersive vibrational bands in thin metal films within a range of fill factors due to the excitation of surface plasmons. The former effect is more relevant at high adsorbate coverage and affects both IRAS and ATR-SEIRAS, while the latter has the same origin as SEIRA (see above) and, therefore, often appears coupled to it.

There are four main consequences of dipole-dipole coupling, which can be easily understood within the relatively simple HEF (Hammaker, Francis and Eischens) model, developed for the particular case of CO adsorbed on Pt.[98] These are:

1. Increase of the vibrational frequency with increasing coverage: As dipoles oscillating at the same frequency come closer to each other at higher coverages, the oscillating electric field generated by one dipole interacts with the oscillating fields of the neighboring dipoles. The consequence is that all dipoles end up oscillating in phase, which results in an effective increase of the corresponding mode's force constant and, thereby, an increase in the stretching frequency. This must not be confused with the change of stretching frequency of an adsorbate with the electrode potential (often called vibrational Stark effect), which will not be discussed here, and often increases if the coverage of an adsorbate is potential dependent.
2. Intensity borrowing between modes oscillating at similar frequencies, by which a mode oscillating at a higher frequency steals intensity from other dipole oscillating at a lower frequency: At sufficiently high (local) coverage, this effect becomes so large that even a small fraction of the higher-frequency species will dominate the spectrum.
3. Inhomogeneous broadening. This is a consequence of the previous effect: as a higher-frequency mode steals intensity from nearby lower-frequency modes, the latter appear as a long tailing at the low frequency side of the band.
4. Lack of proportionality between integrated band intensity and coverage at high coverage: This is partly a consequence of intensity borrowing, and partly due to depolarization effects when several dipoles oscillate next to each other, which effectively results in a decrease of the dynamic dipole moment and, therefore of the intensity of absorption. In general, coverage is proportional to the integrated absorption only at low coverages. At high coverage the dependence flattens out and, at very high coverage, absorption can even decrease with increasing coverage.[99]

In general, the magnitude of dipole-dipole coupling depends on (i) the dynamic dipole moment of the adsorbed species (it is greatest for strongly absorbing modes), (ii) the coverage and (iii) the difference between the frequencies of the oscillating dipoles. For a strongly absorbing mode, like the C–O stretching of adsorbed carbon monoxide, dipole-dipole coupling is small when the bands are more than 100 cm^{-1} apart, but still noticeable even when the oscillator frequencies are separated by as much as 200–300 cm^{-1}, leading, *e.g.*, to CO adsorbed on-top to always appear as the most intense band in infrared spectra of high-coverage CO adlayers on Pt(111), even if CO adsorbed on two-fold or three-fold hollow sites is the majority species.[100] Therefore, care must be taken when making conclusions regarding the coverage or changes in coverage of adsorbates from IR spectra, although the effect will be weaker for less strongly absorbing species.

Coupling between vibrational modes and surface plasmon resonance when working with rough surfaces or nanoparticulate deposits can result in bipolar or anti-absorbance bands[101–107] (*i.e.*, bands in which excitation of an adsorption mode results in an increase, instead of a decrease, of the reflectance of the surface). These bands have often been called *abnormal*,[108] despite being perfectly predictable by Fresnel's reflection laws.[42,43] This phenomenon arises when the IR absorbing species is adsorbed on a moderately reflecting surface, and is therefore associated with the possibility that the amplitude of the component parallel to the interface of the electric field of the standing wave resulting from the interference of the incident and reflected beams is not zero. In IRAS, bipolar and, particularly, inverted bands, are therefore associated with a collapse of the surface selection rule, whereby adsorbed species become visible to *s*-polarized light.[107]

As has been mentioned above, the SEIRA effect also requires a substrate with a moderate reflectivity on which the component parallel to the interface of the electric field of the standing wave is non-zero and, therefore, SEIRA and abnormal band shapes often come together.

The occurrence of these *abnormal* bands depends on the absorption coefficient of the absorbing species (they are favored with strong absorbing species like CO), the fill factor of the metal particles (rather than their size) and the angle of incidence (as would be expected for a phenomenon due to the excitation of plasmons by photons). Both SEIRA and *abnormal* shapes are maximum around the percolation threshold (*i.e.*, the fill factor at which long range connectivity through the nanoparticulate film is attained). This, together with the conductivity of the metal film, has to be taken into consideration when preparing metal films on an IR-transparent substrate for ATR-SEIRAS experiments, as we will illustrate below with the help of Fig. 5.

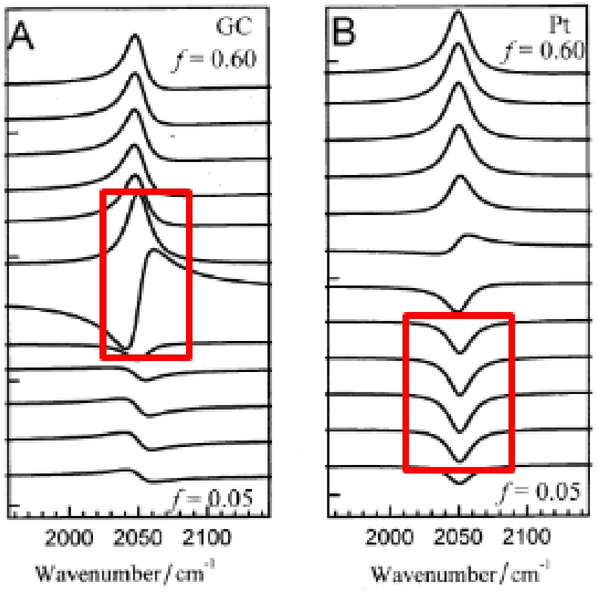

Figure 5. Calculated relative reflectance change at the solid/water interface, $\delta R/R$, due to the adsorption of CO on Pt nanoparticles deposited on glassy carbon (a) and on smooth Pt (b). The fill factor (volume fraction of the composite occupied by the metal particles) of the particles increases from f = 0.05 (bottom) to 0.60 (top) in 0.05 incremental steps. IRAS configuration. The incoming radiation is p- polarized and the angle of incidence at the solid/water interface is 70°. Each division of the ordinate axis corresponds to $\delta R/R$ = 0.1. The spectra have been displaced vertically for clarity. From [42]

Fig. 5 shows the relative change in reflectance due to the adsorption of CO on Pt at the electrode-electrolyte interface calculated using Bruggeman's effective medium approximation,[109] for which the percolation threshold corresponds to a fill factor of 0.33, for different fill factors.[42] Fig. 5(a) would be representative of very thin films on an IR-transparent substrate, whereas Fig. 5(b) is representative of a rough deposit of metal islands on a continuous and smooth metallic film. The latter would be the most appropriate situation for electrochemical experiments, as it would correspond to a metal film with a sufficiently low electrical resistance of at most a few tens of ohms. Fig. 5(a) shows that maximum enhancement is only achieved with very thin metal films at and just above the percolation threshold (red rectangle in Fig. 5(a)). However, very distorted bands or inverted absorption bands would be obtained with these films at or just above percolation, respectively, which might make interpretation of, and extraction of quantitative information from, spectra difficult (in addition to having high resistances in the kΩ region unsuitable for high-quality electrochemical experiments). A thicker, continuous film with a high roughness is better suited for ATR-SEIRAS, despite the lower enhancement achieved (Fig. 5(b)). Enhancement increases with increasing roughness (increasing fill factor of metal islands on a metal film), but when percolation of the metal islands on the underlying homogenous film is reached, a transition from absorption to anti-absorption bands will happen again. This transition will rarely be observed in ATR-SEIRAS, because the metal film will most likely become thicker than the penetration length of the evanescent wave before the threshold is reached, but has been commonly seen in IRAS, *e.g.*, with platinized platinum.[55]

An exception to the rule above applies for ultrafast electrochemical 2D-IR ATR-SEIRAS.[110,111] In this case the intensity of the signal and avoiding heating of the sample by the intense laser pulse are critical, which implies maximizing the enhancement factor and minimizing absorbance of the IR beam by the metal film. Films much thinner (0.1–2.5 nm) than those used in conventional ATR-SEIRAS (20–50 nm) are required, despite their high resistance and the possibility of generating *abnormal* bands.

3. Experimental details of infrared spectroscopy at electrode-electrolyte interfaces

3.1. Selection of windows and angle of incidence

As discussed in Section 2, in IRAS the angle of incidence at the interface has a strong effect on the intensity of the electric field of the standing wave generated by interference of the incident and reflected beam and, through it, on the intensity of absorption bands of adsorbates. In the ATR configuration, the angle of incidence will affect the penetration depth of the standing wave (see Eq. 2), and thus the ability of ATR to detect species in solution. In ATR-SEIRAS, the angle of incidence also has an effect on the intensity of adsorbate bands (although, as will be discussed below, the origin of this effect is different to that of the similar effect in IRAS). Therefore, selecting the most appropriate angle of incidence is critical in order to maximize the sensitivity of both IRAS and ATR-SEIRAS.

Although in principle any IR transparent material can be used as a window in IRAS, as long as it is not soluble in the used solvent, it is preferable to use materials with a refraction index as close as possible to that of water in order to minimize reflection at the window-electrolyte interface. Fluorite (CaF_2) is the most widely used material. In the early days of IRAS, flat windows were employed,[31] but these were soon substituted by triangular prisms or hemicylinders, which allow for normal incidence at the air-window interface, thereby minimizing energy loses by reflection either at the entry or exit point. Furthermore, using flat windows, the angle of incidence at the air-window interface cannot be higher than the corresponding Brewster angle (θ_B = 52º at 1000 cm^{-1}), which limits the highest possible angle of incidence at the electrode-electrolyte interface around 40º, that is far from optimal (see Fig. 2c).

When using prismatic or hemicylindric windows, the angle of incidence at the window-electrolyte interface has to be kept below the critical angle, which for CaF_2 windows is between 70º and 90º in the spectral range between 4000 and 1000 cm^{-1}. If the window is a triangular prism (the most common choice), when the IR beam incides on one of the rectangular faces of the prism at normal incidence, it will reach the adjacent rectangular face with an angle of incidence that will coincide with the angle between the faces involved. Good choices in the case of fluorite are an equilateral triangular prism or a triangular prism beveled at 65°. At 1250 cm^{-1}, and if an equilateral triangular flurorite prism is used, the angle of incidence at the electrode–electrolyte interface is about 64°. The lack of reflection losses at the air–window interface and the higher electric field strength at the electrode surface due to the higher angle of incidence combine to yield a signal-to-noise ratio higher than that achievable using a flat fluorite window. When using hemicylindrical windows, the incidence is always normal at the air–window interface, which makes them most appropriate for studying the effect of the angle of incidence. It has to be noted, however, that such a window will act as a lens, and will displace the position of the focal point of the infrared beam.

In the ATR configuration, the angle of incidence at the window–electrolyte interface must be above the corresponding critical angle. For this reason, high-refractive index materials are the most adequate, with Si and Ge being the most popular choices. Again, prismatic or hemicylindrical windows are preferred to planar windows in order to minimize reflection losses at the air–window interface and thus improve the signal-to-noise ratio. Germanium allows measurements down to 700 cm^{-1}, but has a narrower electrochemical window, which is due to oxidation and dissolution at positive potentials which distort the infrared spectrum.[112,113] Nevertheless, this is not a problem for studies of CO_2 reduction, where rather negative potentials are applied, and Ge provides access to a lower wavenumber region than Si.[114,115]

Silicon is one of the most commonly employed IREs for electrochemical studies. Commercially available multiple-reflection 5 mm thick silicon IREs are not recommended because nearly all the infrared radiation below 1500 cm^{-1} is absorbed by the lattice phonons.[116,117] A single bounce prismatic IRE with the geometry described in the following paragraph is preferred, and enables measurements down to 1150 or 1000 cm^{-1} due to the reduction of the distance travelled by the IR radiation inside the crystal.[118] Micromachined silicon wafers might allow the ability to extend the spectral range as far down as 600 cm^{-1}.[118] In addition, silicon offers very consistent IR signals for a broad range of potentials in acidic and neutral environments, but in highly alkaline environments and at anodic potentials soluble products might form and cause peeling or local delamination of the thin metal film. Although with Si and Ge $\theta_c \simeq 20 - 30$º, equilateral triangular prisms with an angle of incidence considerably higher than θ_c are typically used. In principle, as illustrated in Fig. 2(e), higher incidence angles between 70° and 80º would be preferable. However, due to the expansion of the beam on the interface along the incidence direction and, for the typical electrode sizes of 1–2 cm in diameter, no significant improvement of the band intensity is achieved when the angle of incidence is varied between 60° to 80°. Using an angle of incidence of 60° or 65° has, in addition, the practical advantage that the same reflectance accessory can be used for external reflectance IR spectroscopy and for ATR–SEIRAS.

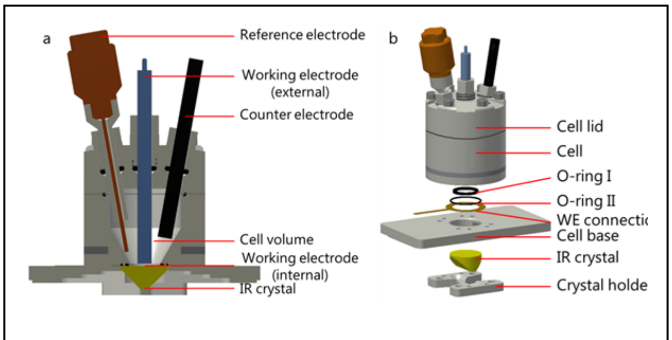

Figure 6: a) Spectro-electrochemical cell that can be used interchangeably for ATR-SEIRAS and RAIRS studies. b) Disassembled view of the spectro-electrochemical cell

3.2. Design of the spectroelectrochemical cell

There are many different cell designs in the literature to collect high quality spectra under operando electrochemical conditions.[119] The design of a spectro-electrochemical cell that can be used interchangeably in internal and external geometry will be presented here (Fig. 6).

When used for ATR-SEIRAS, the metal film on the IRE is the working electrode (WE), while in the case of IRAS, the WE is usually a metal disc introduced into the cell from the top and pressed against the fluorite window. In order to avoid

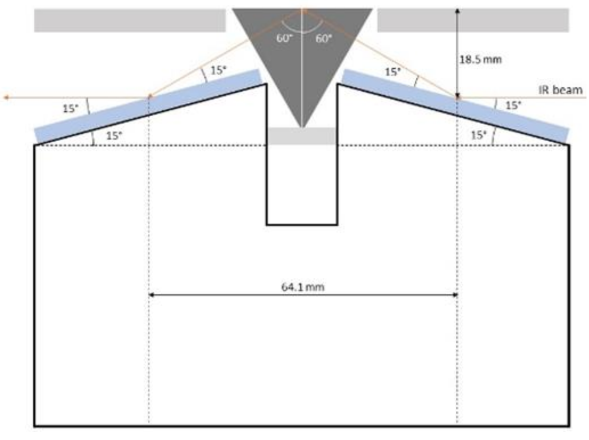

Figure 7: Diagram of a home-made one-reflection reflectance accessory. Although the lack of a focusing lense implies that the sample is not located at the beam's focal point, energy losses due to multiple reflections are minimised.

contamination by ions leaking from the reference electrode (RE, relevant, *e.g.*, when using KCl-saturated Ag/AgCl or SCE as reference for experiments in Cl^--free electrolytes) it is recommended to place the RE in a separate compartment. In order to minimize ohmic potential drops, connection between the RE- and main compartments using a Luggin capillary with its tip placed as close as possible to the WE. Since the WE surface is usually larger than the IR probed area, the reference electrode can be placed outside of the probed area, thereby minimizing the disruption to the current distribution at the probed surface. A coiled Pt wire with a total surface area larger than that of the WE is often used as the counter electrode (CE). Recent studies have shown, however, that, due to the very positive potentials reached at the CE when large cathodic currents are flowing through the WE (as is usual in CO_2 reduction) Pt can dissolve from the CE and deposit on the WE.[120,121] This may cause the working electrode to produce hydrogen preferentially, which is undesirable when probing other chemical reactions such has CO_2 reduction. It is therefore highly recommended to use a wire of the same material as the WE, when possible, or to use high purity carbon based electrodes as the CE.[119]

A tube immersed into the electrolyte can be used to purge the solutions with an inert gas or to saturate it with CO_2. Due to the short penetration depth of the evanescent wave into the electrolyte in the ATR configuration and the trapping of a thin layer of electrolyte between the electrode and the window in IRAS, agitation due to gas bubbling does not perturb the spectra, even when it is intense. In fact, agitation of the electrolyte due to gas bubbling can even help to keep a homogeneous composition in the electrolyte during operation and to increase the transport of reactants to the electrode surface, albeit in an uncontrolled manner. It is sometimes necessary to achieve a better control of the transport conditions, as the local pH and CO_2 concentration can have a critical impact on the activity and product distribution of CO_2 reduction.[122,123] In that case, designs of spectroelectrochemical flow cells can be found in the literature both for ATR and for IRAS. In the latter case, flow cells can be fabricated by drilling a hole either in the center of either the window or the electrode, or by placing a Teflon spacer with injection ports between the electrode and the window.[124] With any of these setups, a pressurized electrolyte can be forced to flow through the thin gap between the electrode and the window and continuously replenish the electrolyte trapped there. Please note that, in this case, even though transport conditions are improved, the problem of the high electrical resistance associated to the thin layer configuration remains.

After assembling the spectroelectrochemical cell, it needs to be placed on top of the sample compartment of the spectrometer, which needs to be equipped with a reflectance accessory designed in such way that it sends the IR beam to reach the side of the prismatic window at normal incidence, and to reach the central area of the window-electrolyte interface. Fig. 7 shows an illustration of a simple one-reflection home-made accessory designed for equilateral triangular prisms. Commercially available accessories fit most of the more common commercial spectrometers, and often allow manipulation of the angle of incidence.

Due to the small amount of matter typically sensed (a full monolayer corresponds to approximate 1 nmol of adsorbate per cm^2 of real area), extreme care has to be taken to avoid the strong IR absorbance by H_2O vapor and CO_2 in the atmosphere. All the beam pathway, including the sample compartment containing the reflectance accessory, has to be purged with CO_2-free dry air or vacuum pumped. The attachment of the cell to the sample compartment has to be airtight and the sides of the window through which the beam enters and exits the cell must be located inside the purged sample compartment.

4. Applications in the electrocatalytic reduction of CO_2

Elucidation of the reaction mechanism of CO_2 electroreduction can bring fundamental insights that can allow further control over selectivity, activity and stability of an electrocatalyst. The reaction mechanisms in aqueous media have been thoroughly investigated both theoretically and experimentally.[3,125] Online and offline experimental studies on single-crystal electrodes,[16,126–129] polycrystalline materials[130] and well-defined nanoparticles[131] by combining electrochemical techniques with chromatography and different spectroscopies have delivered crucial information regarding reaction products, and eventually indirect information on reaction intermediates. For a detailed description of the subject, the reader is referred to earlier reviews.[21,132] However, there remain substantial discrepancies regarding the nature of the intermediates and the rate determining steps for each one of the detected reaction products.[3,133] Monitoring known or possible surface bound intermediates, *e.g.* CO, acetaldehyde, -COOH or -COH by using in-situ IR spectroscopy could potentially provide highly important information to test and refine the proposed mechanisms. However, this task encounters serious complications that need to be well known and taken into account in order to prevent the erroneous interpretation of spectroelectrochemical experiments.

4.1. Band assignment: masking of CO_2 in solution by $CO_2(g)$

Even when using ATR-SEIRAS, which is considerably more sensitive to adsorbed species than to species in solution due to the thin layer of electrolyte probed and the short range of the SEIRA effect, dissolved CO_2 in the vicinity of the electrode surface can be detected due to its very large IR absorption cross section. In-situ infrared spectroscopy thereby allows the ability to correlate the current with the decrease in CO_2 concentration. Care has to be taken, though, not to mistake atmospheric CO_2 ($CO_2(g)$), which can be present in the sample or even the optical and detector chambers of the spectrometer unless very efficiently purged, for dissolved CO_2 (usually denoted $CO_2(aq)$ in the case of aqueous solutions), which has been shown to be the actual reactive species.[121] It is thankfully quite easy to distinguish between atmospheric CO_2 and dissolved CO_2, the latter being the reactive species in CO_2 reduction, although this has unfortunately not prevented the former to be mistaken for the latter too often. Excitation between quantized rotation levels is possible in the gas phase, but not when CO_2 is dissolved. Consequently, aqueous CO_2 appears as a single peak with maximum at 2343 cm^{-1}, while in the gas phase CO_2 shows a doublet with peaks just above and below 2343 cm^{-1}, respectively. The presence of a double peak in the spectra is clear evidence that CO_2 in the gas phase is being probed.

In the gas phase, infrared simultaneously provokes transitions between vibrational levels and rotational levels. At room temperature, only the fundamental vibrational state is occupied, and since the infrared selection rule dictates that only transitions between adjacent vibrational levels are allowed ($\Delta\nu = \pm 1$), only the fundamental vibrational transition is usually observed. On the contrary, at room temperature many of the available rotational levels are occupied, and any transition between any occupied rotational level and those immediately above or below is possible ($\Delta J = \pm 1$). This usually results in three branches in the infrared spectra of gaseous molecules: (i) a P branch at frequencies lower than the fundamental vibrational transition, corresponding to those transitions in which the increase in the vibrational level is accompanied by a decrease to the next lower rotational level ($\Delta J = -1$); (ii) an R branch at frequencies higher than the fundamental vibrational transition, corresponding to those transitions in which the increase in the vibrational level is accompanied by an increase to the next higher rotational level ($\Delta J = +1$); and (iii) a Q branch, corresponding to those transitions in which the increase in the vibrational level is not accompanied by a change in the rotational level ($\Delta J = 0$; this branch appears, hence, exactly at the vibrational transition wavenumber). The latter are only possible if the molecule has angular momentum about its axis, otherwise the Q branch is absent. CO_2 lacks such an angular momentum and, consequently, the IR spectrum of gaseous CO_2 shows no absorbance at 2343 cm^{-1}, the fundamental frequency of its antisymmetric stretching. In the P and R branches, rotational-vibrational transitions are separated by $2B$ cm^{-1}, with B the molecule's rotational constant. In the case of CO_2, $B = 0.390$ cm^{-1},[134] and the separation between lines is of only 0.78 cm^{-1}, too small to be resolved with the typical spectral resolutions of 4 or 8 cm^{-1} used in IR spectroelectrochemical experiments. This results in two broad bands above and below the fundamental frequency, with maximum frequencies corresponding to the transition from the most populated rotational level to that immediately above and immediately below it, respectively. On the contrary, in the liquid phase molecules are unable to rotate freely, and the rotational structure of vibrational spectra is blurred, resulting in a single line centered at the fundamental vibrational frequency (2343 cm^{-1} in the case of CO_2).

Due to insufficient purging of the spectrometer's sample (and sometimes also optical and detector) chamber, $CO_2(g)$ bands are often accompanied by clear vibrational spectra of water vapor in both the ν_{O-H} and δ_{O-H-O} regions. These bands, particularly the latter, centered at 1610 cm^{-1} but extending up to 1800 cm^{-1}, have a detrimental effect on the quality of in-situ IR spectra, as they increase the noise and can easily obscure small bands due to products and intermediates appearing in the region affected.

4.2. Band assignment: mistaking CO_3^{2-} and HCO_3^- with adsorbed intermediates

The electroreduction of CO_2 is a proton-electron transfer reaction, consuming protons or releasing OH^- ions depending on the pH. Unless working in clearly acidic or alkaline conditions, or using hydrodynamic methods (*e.g.*, the rotating-disk electrode, RDE), which allow for fast replenishment of consumed protons, the local pH at the electrode-electrolyte interface will always increase during CO_2 reduction. The fact that, at least in aqueous solutions, hydrogen evolution nearly always (if not always) accompanies CO_2 reduction, also contributes to the increase in the local pH. Obviously, the effect is stronger around pH 7, and using a buffer will minimize but not cancel it.[15]

The most commonly used buffer for CO_2 reduction is CO_2-saturated bicarbonate solutions, because, in addition to having a pH of around 6.5, it can act as a reservoir of CO_2 in the form of HCO_3^-. As has been explained in sections 2.2 and 2.3, even though SEIRA is particularly sensitive to surface species, it is also sensitive to species at a distance from the electrode surface short enough for them to interact with the evanescent wave, particularly if they are strong IR absorbers, as is the case of CO_2, HCO_3^- and CO_3^{2-}. Starting with carbonate and bicarbonate free solutions is not helpful since CO_2 can react at the surface with cathodically produced hydroxide ions.

There have been a considerable amount of recent studies claiming the identification of intermediates such as *COOH, *COO or *COH during the reduction of CO_2 on different metals.[135,136] These species have also been proposed as intermediates in the electrooxidation of small organic molecules like methanol and formaldehyde, and attempts of detecting them using in-situ IR spectroscopy date back to the very first applications of the technique.[137,138] However, with only one exception, namely, the detection of adsorbed formyl (*COH) on Pt during the electrooxidation of formaldehyde,[139] no convincing evidence of the presence of any of those intermediates on the electrocatalyst surface has ever been found. Even in the case mentioned above, the intensity of the signal attributed to adsorbed formyl was very low,[139] which is actually to be expected for any of the species indicated above, as their steady-state coverage must be low and, furthermore, their most characteristic vibrational mode, that corresponding to the C=O stretching, will lie at around 120º from the surface normal. The bands expected for these reaction intermediates fall within the region in which bicarbonate and carbonate vibrational modes, as well as the bending mode of water, are active. As discussed above, slight changes in interfacial pH during the electroreduction of CO_2 can lead to significant changes in the concentrations of bicarbonate and carbonate at the interface, which will result in bands which could be easily mistaken for those species. If, in addition, we take into account that adsorption of carbonate and bicarbonate on metal surfaces is possible even in acidic media[140,141] (which will lead to an increase in the number of their bands due to rupture of the degeneracy of some vibrational modes because of the reduction of the molecule's symmetry upon adsorption, as well as to a shift in frequencies compared with those corresponding to the solvated ions), the number of bands due to (bi)carbonate species that can appear in this spectral region is even larger. It is important to note that although the adsorption of (bi)carbonate on a metal electrode at the very negative potentials needed for CO_2 reduction is unlikely, adsorbed (bi)carbonate might still have been present at the positive potentials often used to record the reference spectrum when analyzing this reaction, leading to negative absorption bands after desorption at the negative sample potentials. Overlapping of negative- and positive-going bands due to a combination of anion desorption and concentration changes at the interface can result in difficult-to-interpret spectra and, in general, assignment of bands to these reaction intermediates has to be done with extreme caution.

4.3. Brief review of recent work

CO_2-saturated bicarbonate solutions are often used as electrolytes for CO_2 reduction because they constitute buffers with a pH around 7.[15] As discussed in the preceding section, the buffering capacity of these solutions is not sufficient to avoid the increase of the pH near the electrode surface during the reaction,[142] and intensity and frequency of the bands may change with the concentration of HCO_3^- and CO_3^{2-} that can obscure or be mistaken for intermediate species. However, this disadvantage can be turned into an advantage, and be used to determine the local pH at the interface in *operando* conditions. Ayemoba and Cuesta[48] used ATR-SEIRAS to experimentally determine the pH at the electrode-electrolyte interface during the electroreduction of CO_2 by determining the ratio between the integrated areas of the absorption bands corresponding to CO_2 and HCO_3^-. Using gold films chemically deposited on silicon, they demonstrated that, at a given potential, the increase in the pH near the electrode surface follows the sequence $Li^+ > Na^+ > K^+ > Cs^+$ (Fig. 8, left), a sequence which is not agreement with the commonly observed fact that C_2 products are favored by an alkaline pH near the electrode surface .[4,8,143–145] Nevertheless, this provided experimental support to a previous hypothesis by Singh et al.,[146] who attributed the trend above to a decreasing pK_a of hydrolysis of cations at the interface with increasing cation size, due to polarization of the water molecules in the cation's hydration shell. It must be re-emphasized, however, that a higher buffering capacity had been found in other studies to favor production of methane over ethylene,[21] which is in contradiction with Singh's et al.'s hypothesis.[146] However, the local pH depends considerably on the purity of the salt used to prepare the electrolyte, and exactly opposing trends can be found if a set of alkaline-metal carbonates of lower purity is used (see Fig. 8, right panel), which might explain these discrepancies. [48] Nonetheless, the highest pH increase always coincided with the lowest current densities, and vice-versa.

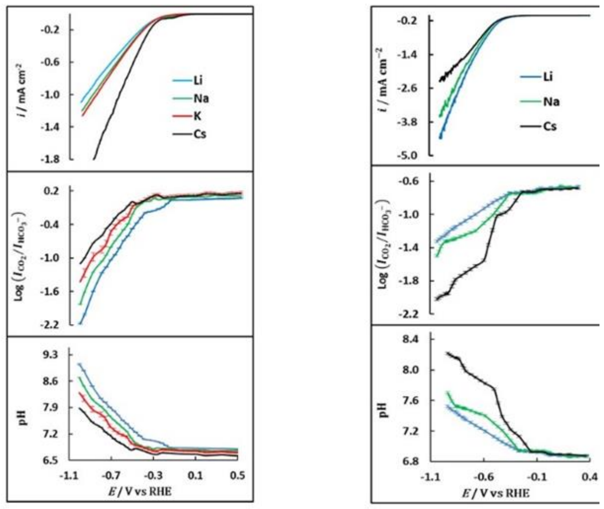

Figure 8: Linear sweep voltammograms at 1 mV s^{-1} (top panels) of a thin-film Au electrode on Si in CO_2-saturated 0.05 M M_2CO_3 solution (M = Li (blue), Na (green), K (red) and Cs (black)) in D_2O, potential dependence of the ratio between the integrated absorbance of the CO_2 and HCO_3^- bands (mid panel), as obtained from simultaneously recorded ATR-SEIRA spectra, and potential dependence of the interfacial pH (bottom panels). The panels on the right corresponds to experiments using a different set of M_2CO_3 to prepare the solutions, of lower purity. From [48]

Dunwell et al. measured the concentration at the cathode surface of bicarbonate, carbonate and CO_2(aq) during CO_2 electroreduction with improved and well-controlled transport conditions.[147] After reaching a steady-state current at a given applied potential, the ratio of the integrated areas of bicarbonate and carbonate were used to determine the pH near the electrode surface. The increase of the pH near the electrode surface leads to an extra concentration overpotential to overcome. In addition, if there is not enough supply of CO_2 via convection, the concentration of CO_2 near the electrode surface decreases considerably at high current densities, which leads to an additional concentration overpotential. Fig. 9, shows the concentration overpotentials due to H^+ (η_{c,H^+}) and CO_2 (η_{c,CO_2}), as well as the total overpotential, due to the consumption of both H^+ and CO_2 at the electrode surface, as a function of both the electrode potential (Fig. 9(a)) and the current density (Fig. 9(b)). In an unstirred electrolyte, the sum of the concentration overpotentials is around 0.17 V at a potential of -0.8 V vs RHE. Even though stirring the electrolyte and using high buffer capacity solutions substantially decreased the concentration overpotentials on planar electrodes, the mass transport inside the pores of nanostructured electrodes might be different.

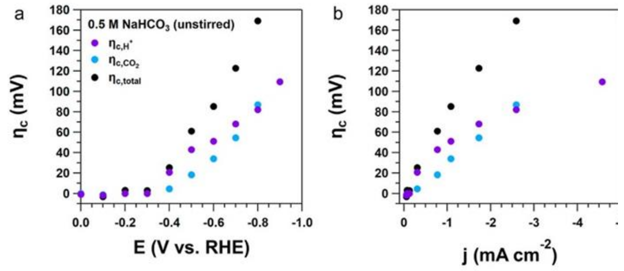

Figure 9: Concentration overpotentials caused by the production of hydroxide and depletion of CO_2 and protons near the electrode surface in CO_2-saturated 0.5 M $NaHCO_3$ as a function of the electrode potential (a) and the current density (b) without stirring. From [147]

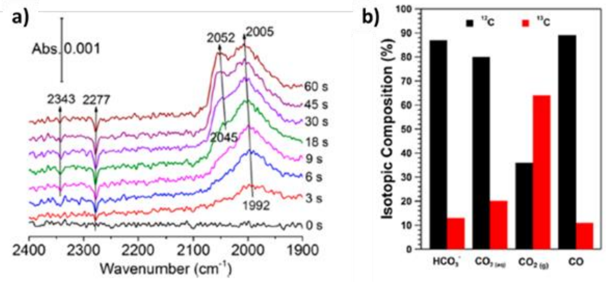

Figure 10: Time resolved ATR-SEIRA spectra obtained during the reduction of CO_2 on Cu in $^{12}CO_2$-saturated 0.1 M $KH^{13}CO_3$ at -0.6 V vs. RHE. From [147]. b) Isotopic composition of bicarbonate, CO_2 dissolved in the electrolyte (CO_2(aq)), CO_2 in the headspace of the electrochemical cell (CO_2(g)) and CO in the headspace of the electrochemical cell after 5 min of electrolysis in $^{13}CO_2$-saturated 0.5 M $H^{12}CO_3$ at -0.6 V vs. RHE with a Au electrode. From [121]

Because CO_2-saturated bicarbonate solutions are the most commonly used electrolytes in electrochemical CO_2 reduction, the role of HCO_3^- in the reaction has been examined in some detail. Experiments in argon-purged bicarbonate solutions suggest that HCO_3^- might be reduced to formic acid either directly or indirectly via its equilibrium with CO_2.[148–150] However, no appreciable amount of other products like, *e.g.*, CO or methane, have been reported when electrolysis is performed under an Ar atmosphere in bicarbonate solutions.[15] Zhu et al.[136] and Dunwell et al.[121] independently studied the role of bicarbonate in CO_2 electroreduction by combining ATR-SEIRAS and isotopic labelling on copper and gold electrodes, respectively. Fig. 10a shows time-resolved spectra collected during CO_2 reduction on Cu at -0.6 V vs RHE in $^{12}CO_2$-saturated $KH^{13}CO_3$.[136] The peaks around 2343 cm^{-1} and 2050 cm^{-1} correspond to $^{12}CO_2$ and ^{12}CO, respectively, while $^{13}CO_2$ and ^{13}CO appear at 2277 and *ca.* 2000 cm^{-1}, respectively. At the beginning of the experiment, ^{13}CO dominates the spectrum, but the ^{12}CO signal gradually increased in intensity until both were of similar magnitude. This was taken as evidence that CO is produced from CO_2 generated from the dynamic equilibrium between CO_2 and HCO_3^-, which is discarded as the actual reactant because no appreciable amount of CO can be detected in the headspace using gas chromatography (GC) after prolonged electrolysis in the absence of CO_2.[121] Detailed experiments combining ATR-SERIAS and mass spectrometry using $^{13}CO_2$-saturated $NaH^{12}CO_3$ allowed an estimation of the isotopic composition of HCO_3^-, CO_2(aq), CO_2(g) and CO after 5 min of electrolysis using a Au electrode at -0.6 V vs. RHE (Fig. 10(b)),[121] which confirmed the relatively rapid dynamic equilibrium between CO_2 and HCO_3^- (only limited by the rate of hydration of CO_2). Remarkably, this result is also strong evidence that the actual reactant is CO_2(aq) rather than CO_2(g), and reveals the importance of adequate purging of the FTIR apparatus as discussed in Section 4.1. It also calls for extreme caution with IR spectra used to assess the reactivity of electrocatalysts for CO_2 reduction based on variations of the intensity of CO_2 bands clearly corresponding to CO_2(g).[151] These two works also confirm the notion that bicarbonate not only acts as an electrolyte but also as a CO_2 reservoir through its dynamic equilibrium with CO_2. This is most likely the reason behind the smaller partial current density of CO_2 reduction in bicarbonate-free solutions.[121,152]

CO is almost certainly the intermediate in the formation of higher order hydrocarbons and alcohols from CO_2 on copper electrodes, although there is no consensus on the rate determining step of the reaction pathway leading to these products.[3,130,153]. For this reason, several recent studies have focused on understanding the adsorption and reduction of CO on Cu. Gunathunge et al.[154] recently used ATR-SEIRAS and SERS to investigate the possibility of a reversible CO-induced reconstruction of the Cu surface, and its effects on the activity and selectivity of Cu for CO_2 reduction. Fig. 11(a) shows a series of spectra collected at different potentials in CO-saturated 0.1 M $KHCO_3$. At low overpotentials, a broad low frequency band (LFB) spanning roughly from 1990 cm^{-1} to 2100 cm^{-1} was observed and attributed to linear CO on low-index facets of the nanoscale copper clusters. Upon polarization to more negative potentials, a sharp high frequency band (HFC) overlapping with the LFB emerged over a narrow potential range, which was attributed to linear CO on

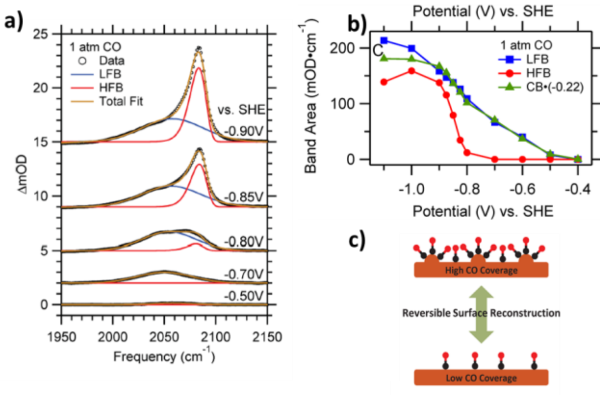

Figure 11: a) Dependence on the electrode potential of the ATR-SEIRA spectrum of CO adsorbed on Cu in a CO-saturated 0.1 M $KHCO_3$ solution. **b)** Evolution with potential of the integrated intensities of the high-frequency and low-frequency components of the band of CO adsorbed on Cu, alongside that of the band corresponding to carbonate species in the solution. **c)** Schematic representation of the potential-induced surface reconstruction of Cu, and how it affects the adsorption site of CO. From [154].

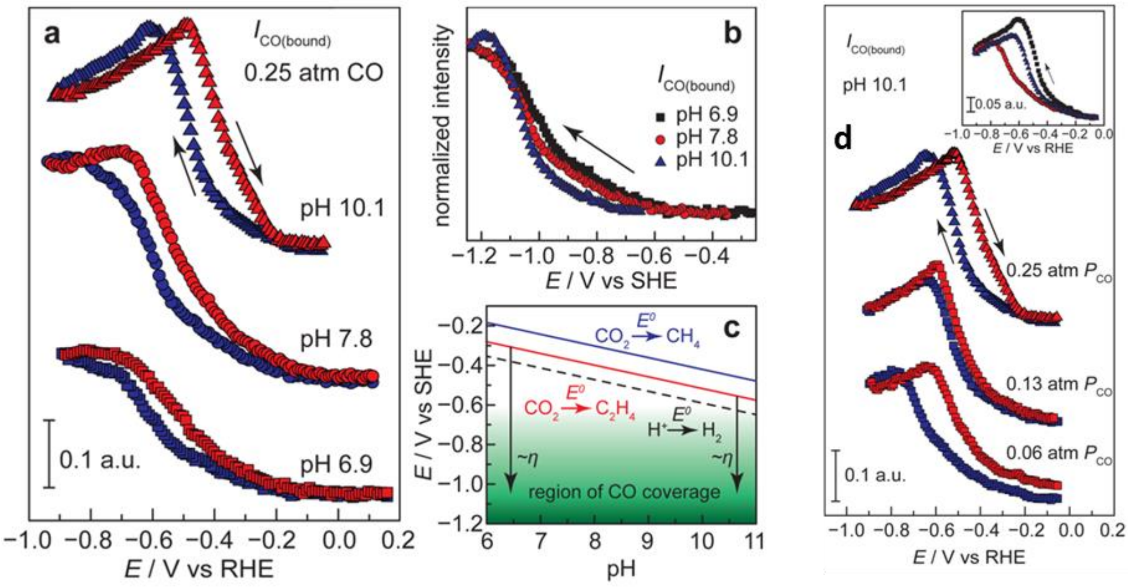

Figure 12: a) Potential dependence of the CO coverage on Cu in 0.1 M (bi)carbonate buffer at pH 6.9 (squares), 7.8 (circles), and 10.1 (triangles), recorded in the presence of 0.25 atm of CO on both the negative- (blue) and the positive-going (red) scans. **b)** Dependence on the electrode potential of the normalized integrated intensity of the CO band in the negative-going scan at pH 6.9 (black squares), 7.8 (red circles), and 10.1 (blue triangles) plotted vs the pH-independent SHE scale. **c)** Pourbaix diagram depicting the region where CO adsorbed on copper can be observed (green region) and the equilibrium potentials for the H^+/H_2 (black dashed line), CO_2/CH_4 (blue line), and CO_2/C_2H_4 (red line) redox couples as a function of pH. Black arrows denote the approximate overpotentials (η) required to reach maximal CO surface concentrations. **d)** Potential dependence of the CO coverage on Cu at pH 10.1 and CO partial pressures of 0.06 atm, 0.13 atm, and 0.25 atm on both the negative- (blue) and positive-going (red) scans. Inset: Overlay of the dependence of the integrated intensity of the CO band in the negative-going scan at CO partial pressures of 0.06 atm (red), 0.13 atm (blue), and 0.25 atm (black). From [161]

defect sites. The evolution of the integrated intensity of the LFB and HFB of CO are given in Fig. 11(b) alongside that of a negative band around 1540 cm^{-1} corresponding to the desorption of HCO_3^-/CO_3^{2-} ions. While the LFB clearly runs in parallel to the HCO_3^-/CO_3^{2-}, suggesting the adsorption of CO on copper is accompanied by desorption of specifically adsorbed anions (in agreement with early reports by Hori et al.[155]), there is no correlation between the HCO_3^-/CO_3^{2-} band and the HFB, which, in addition, increases sharply between -0.8 and -0.9 V. Similar CO bands and a similar evolution of their intensity with potential were found when CO was generated by the reduction of CO_2, and in all cases the emergence of the HFB occurred once the LFB achieved the same threshold intensity. The same bands showing the same potential dependence were observed with SERS, and time-resolved ATR-SEIRAS after a potential step from -0.70 to -1.10 V vs. RHE in CO_2 saturated solutions clearly showed that the LFB forms before the HFB, and that the intensity of the latter is directly proportional to that of the former.[154] All these data suggest a CO-induced reversible surface reconstruction of copper in the potential region where CO_2 reduction occurs (Fig. 11(c)), as had been proposed by Soriaga and co-workers[156–159] based on electrochemical scanning tunneling microscope (EC-STM) experiments.

Several studies suggest that the adsorption of CO on copper is reversible,[154,160] with very little hysteresis between the back and forward scan. This is confirmed by isotopic exchange experiments, in which adsorbed ^{12}CO generated on the surface of a Cu electrode upon polarization at -0.80 V vs. RHE in CO_2-saturated 0.1 M $NaHCO_3$ was readily exchanged by ^{13}CO when the latter was bubbled through the solution,[161] showing that CO adsorbed on Cu is in dynamic equilibrium with CO(aq). This is evidence that CO adsorbs on Cu neither too weakly nor too strongly, providing a route to further hydrogenation.

Wuttig et al.[161] also performed a systematic study of the potential-dependent reversible adsorption of CO on Cu at different pH's (Fig. 12). They found the CO adsorption profiles to shift 0.06 V pH^{-1} in the RHE scale (Fig. 12a), *i.e.*, to be constant in the SHE scale (Fig. 12 b). As the equilibrium potentials for reduction of CO_2 to highly hydrogenated products shift -0.06 V pH^{-1} in the SHE scale (Fig 12c), this implies that, at higher pHs, a higher coverage of CO is achievable at lower overpotentials, which, according to the authors, might explain why reduction of CO_2 to higher order hydrocarbons is generally found to be more facile in alkaline media.[6,20,162] Remarkably, while at pH 6.9 and 7.8 the CO coverage increases with increasing negative potential until reaching a plateau. At pH 10.1 the CO coverage increases up to a maximum, after which it starts decreasing (Fig. 12a). The decrease was shown to be independent of the CO partial pressure (Fig. 12d) and, therefore, not to be due to equilibrium desorption of CO. Instead, the decline in CO population at highly negative potentials for pH 10.1 was considered to be due to the reversible conversion of CO to another surface species. Possible candidates suggested by Wuttig et al. are adsorbed OCCO and adsorbed formyl, but, if present, they eluded detection due to potential overlapping of their bands with those of carbonate species and/or their very weak absorption due to the orientation of their most characteristic vibrational modes. In any case, this fast interconversion between adsorbed CO and the next reaction

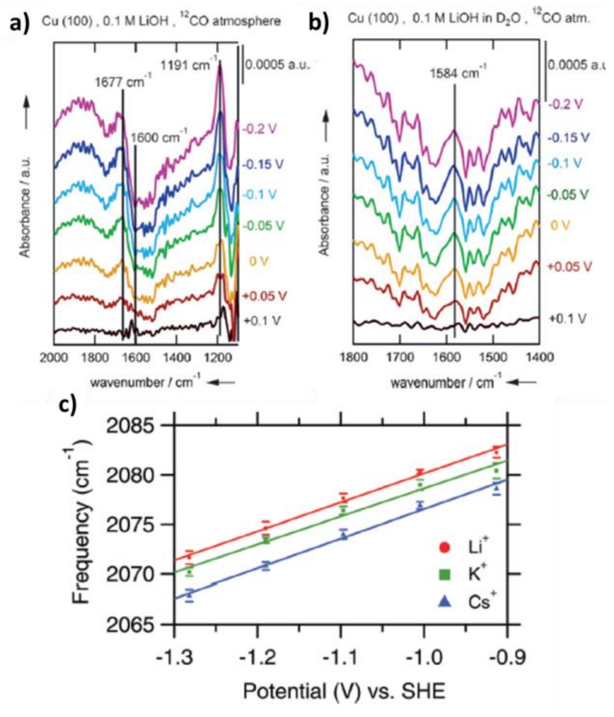

Figure 13: Potential-dependent absorbance spectra for Cu(100) in the absence (a) and presence (b) of CO in a 0.1 M LiOH solution. Reference spectrum recorded at +0.1 V vs. RHE. From [165]. **c)** Peak frequencies of the CO stretching band of linearly-bonded CO on Cu as a function of applied potential in CO-saturated 0.1 M alkali metal bicarbonates as indicated. From [167].

intermediate challenges many proposed mechanistic schemes,[21,125,163,164] according to which the conversion of CO to a dimer or a more hydrogenated intermediate is the rate-determining step in the formation of higher order C_1 and C_2 products.

Perez-Gallent et al.[165] have recently studied the electroreduction of CO in an alkaline medium on Cu(100) electrodes to understand the formation of C_2 products using IRAS. Spectra at increasingly negative potentials in CO-saturated 0.1 M LiOH solutions in H_2O and D_2O are shown in Fig. 13a and 13b, respectively. With the help of DFT calculations, the band at 1191 cm^{-1} was assigned to the COH stretching of the hydrogenated CO dimer intermediate OCCOH. The corresponding CO stretching at 1584 cm^{-1} can only be observed with D_2O, as it is otherwise masked by the H_2O bending mode. Further experiments using ^{13}CO provided additional support to the existence of the hydrogenated dimer, which was considered to be the most stable intermediate leading to C_2 products via a CO coupling mechanism. Considering the dilute nature of these intermediates and sensitivity of IRAS, the low signal to noise ratios in these spectra are understandable. Thereafter, Perez-Gallent et al.[166] used online electrochemical mass spectrometry (OLEMS), high-performance liquid chromatography (HPLC) and IRAS to study the effect of cations on the formation of hydrocarbons from CO in alkaline media. Remarkably, the dimer intermediate OCCOH could only be observed with IRAS at low overpotentials (IRAS studies are limited to very low overpotentials in order to avoid distortion of the spectra by hydrogen bubbles trapped in the thin electrolyte layer between the electrode and the window) in the presence of small cations such as Li$^+$, Na$^+$ and K$^+$, but not Rb$^+$ or Cs$^+$. This observation was supported by DFT calculations, which showed that the former cations were found to stabilize the key intermediates better than the latter. Although this explains the higher selectivity of copper electrodes towards C_2 products at lower overpotentials, it is not clear how it agrees with the higher production of ethylene, for which OCCOH is proposed to be an intermediate, in the presence of Rb$^+$ or Cs$^+$ as compared with Li$^+$, Na$^+$ and K$^+$.

Although differing in the details, the interpretations of cation effects on the activity and selectivity of CO_2 reduction of Singh et al.,[146] Ayemoba and Cuesta[48] and Pérez-Gallent et al.[166] all rest on cation-induced differences in the electric field felt by solvent and intermediate species at the electrical double layer. Gunathunge et al.[167] have studied these effects by examining the effect of the cations on the stretching frequency of CO on Cu using ATR-SEIRAS. Fig. 13c shows the dependence of the stretching frequency of adsorbed CO on the electrode potential for Li$^+$, K$^+$ and Cs$^+$. The CO stretching frequency clearly decreases in the sequence Li$^+$ > K$^+$ > Cs$^+$, which was attributed to an increase in the electric field felt by the CO molecule following the sequence Li$^+$ < K$^+$ < Cs$^+$.

In-situ IR spectroscopy has also been used to study the electroreduction of CO_2 in non-aqueous media. Non-aqueous media, like electrolytes based on organic solvents or ionic liquids, often have wider potential windows than aqueous electrolytes, allowing the ability to reach very negative potentials without the competing HER. In addition, gases like CO_2 are typically an order of magnitude more soluble in organic solvents than in water. It is important to note, however, that, from a practical point of view, dry non-aqueous media are not the most appropriate for the reduction of CO_2 to useful products, as this involves a series of proton-electron transfers and, consequently, a good proton donor is required. In the absence of a proton donor, the only possible products are oxalate (resulting from the coupling of two CO_2^- radicals) or CO and carbonate (resulting from the disproportionation of the CO_2^- radical, $2CO_2^- \longrightarrow CO + CO_3^{2-}$).

Figueiredo et al.[168] used IRAS to study the electroreduction of CO_2 on copper in *wet* acetonitrile, where CO and bicarbonate (due to the local increase in pH, as discussed above) were mostly observed as products. Similar results were obtained with Pt, Pb, Au, Pd, and Ag electrodes. For all electrode materials, mostly bicarbonates were observed as products due to the reduction of water traces. Oxalate was only observed on Pb electrodes at very high overpotentials.

Rudnev et al.[169] used ATR-SEIRAS to study the electroreduction of CO_2 on gold. They assigned a very intense band at 1623 cm^{-1} to the CO_2^- radical, however, based on the results of Figueiredo et al.,[168] it seems more likely to correspond to the formation of bicarbonate. An interesting observation was the detection of a band whose frequency redshifted with increasingly negative potential from 2127 and 2085 cm^{-1} and which appeared both in the presence and absence of CO_2. The authors tentatively assigned this band to adsorbed cyanide on gold formed by the reduction of acetonitrile. These results highlight the importance of a previous, detailed, examination of the reactivity of non-aqueous solvents before attempting any electrocatalytic study, as bands resulting from solvent decomposition could otherwise easily be mistaken for products of the electrocatalytic reaction.

Papasizza and Cuesta[170] have recently reported an ATR-SEIRAS investigation of the electroreduction of CO_2 on a Au electrode in an 18% 1-ethyl-3-methylimidazolium tetrafluoroborate ([EMIM]BF_4)/water (mol/mol) mixture. They showed that the electroreduction of CO_2 results in the formation of CO_{ad}, whose coverage increases with increasing negative potential, and appears to establish an equilibrium with dissolved CO in the electrolyte. Interestingly, ATR-SEIRAS revealed the presence of two types of water in the [EMIM]BF_4/water mixture, with different degrees of hydrogen bonding, which they attributed to water in water-rich regions (bulk-like water) and water in an RTIL-rich environment. In the presence of CO_2, only bulk-like water accumulates at the interface at negative potentials, while water associated with an RTIL-rich environment is depleted from it. This was considered as an indication that this kind of water might be preferentially used as a proton donor for the reduction of CO_2.

5. Challenges and opportunities

In situ and *operando* IR studies applied to CO_2 electroreduction have significantly increased in the last decade. The ability to directly observe reaction intermediates is one of the key objectives of combining infrared spectroscopy and electrochemistry, but is complicated by interference with solvent and electrolyte species.

One of the limitations of IR at the electrode-electrolyte interface is the limited accessibility to low wavenumbers. In the particular case of ATR-SEIRAS, a single bounce with Si windows allows the ability to circumvent absorption by Si phonons and extend the spectral window down to 1000 cm^{-1}, but accessing lower wavenumbers would improve the analysis of vibrational modes and might provide access to structural information regarding the surface oxides and hydroxides. Recently, it has been shown that micromachined Si wafers allow measurements down to 600 cm^{-1} by minimizing the path that the infrared beam travels inside the IRE.[171] These wafers are commercially available and can be used in ATR-SEIRAS measurements to access low wavenumbers.[172]

Another drawback of ATR-SEIRAS is that the thin metal films deposited onto the IRE are usually polycrystalline and do not allow the ability to study the effect of surface structure on the activity and selectivity of the reaction. Although, on the contrary, IRAS can be used for single-crystal studies, this geometry suffers from several limitations associated to the thin layer configuration. The enhancement in SEIRA is usually due to randomly oriented nanoparticles that produce plasmon resonances with a broad absorption mainly in the visible range, with minor infrared absorption. Higher enhancements (~ 5 orders of magnitude) have been achieved by using metal nanoantennas where the spectral range of plasmon enhancement can be engineered by controlling their aspect ratio and geometry.[173] Although the enhancement occurs in only a narrow part of the infrared spectrum (typically a few µm), the range can be made compatible to the spectral region of interest for CO_2 reduction applications. The technique was first demonstrated in 2008 by Neubrech et al. on dry samples,[87] and has been later modified for in situ applications in water.[174] Since metal nanoantennas are isolated nanostructures, electrochemical applications are challenged by the discontinuity and conductivity of the metal layer. A way to overcome this would be by creating nanogaps or slits rather than nanostructures.[175] In this way, a continuous film with periodically placed slits could be used as the active enhancement material in electrochemical applications.

In conclusion, *in situ* IR techniques are important tools to elucidate the reaction mechanism of CO_2 reduction and other electrochemical processes, however, their application is challenging and not free of practical and technical problems. Still, they can provide extremely useful information to help the field improve the incomplete status of knowledge about the nature of reaction intermediates involved in the reduction of CO_2, the relevance of double layer effects in controlling the activity and selectivity of the electrocatalysts, as well as the nature of the species causing deactivation. Recent advances in instrumentation, plasmonics and nanoscience will hopefully help us enhance the capabilities of IR-based techniques in terms of sensitivity and time resolution.

Acknowledgements

Recep Kas and Wilson A.Smith thanks to European Research Council (ERC) fort he financial support under the European Union's Horizon 2020 research and innovation programme (grant agreement no. 759743 – WUTANG).

Keywords: In-situ infrared spectroscopy • electrochemical CO_2 reduction • spectro-electrochemistry • SEIRAS • Carbon Dioxide

REFERENCES

[1] G. A. Olah, G. K. S. Prakash, A. Goeppert, *J. Am. Chem. Soc.* **2011**, *133*, 12881–12898.

[2] E. V. Kondratenko, G. Mul, J. Baltrusaitis, G. O. Larrazábal, J. Pérez-Ramírez, *Energy Environ. Sci.* **2013**, *6*, 3112.

[3] A. M. Appel, J. E. Bercaw, A. B. Bocarsly, H. Dobbek, D. L. DuBois, M. Dupuis, J. G. Ferry, E. Fujita, R. Hille, P. J. A. Kenis, et al., *Chem. Rev.* **2013**, *113*, 6621–6658.

[4] Y. Hori, S. Suzuki, *Bull. Chem. Soc. Jpn.* **1982**, *55*, 660–665.

[5] Y. Hori, K. Kikuchi, A. Murata, S. Suzuki, *Chem. Lett.* **1986**, *15*, 897–898.

[6] Y. Hori, A. Murata, R. Takahashi, *J. Chem. Soc. Faraday Trans. 1* **1989**, *85*, 2309–2326.

[7] T. E. Teeter, P. Van Rysselberghe, *J. Chem. Phys.* **1954**, *22*, 759–760.

[8] W. Paik, T. N. Andersen, H. Eyring, *Electrochim. Acta* **1969**, *14*, 1217–1232.

[9] K. S. Udupa, G. S. Subramanian, H. V. K. Udupa, *Electrochim. Acta* **1971**, *16*, 1593–1598.

[10] J. Ryu, T. N. Andersen, H. Eyring, *J. Phys. Chem.* **1972**, *76*, 3278–

3286.

[11] U. Kaiser, E. Heitz, *Ber. Bunsenges. Phys. Chem.* **1973**, *77*, 818–823.

[12] S. Meshitsuka, M. Ichikawa, K. Tamaru, *Chem. Commun.* **1974**, 158.

[13] P. G. Russell, N. Kovac, S. Srinivasan, M. Steinberg, *J. Electrochem. Soc.* **1977**, *124*, 1329.

[14] R. Williams, R. S. Crandall, A. Bloom, *Appl. Phys. Lett.* **1978**, *33*, 381–383.

[15] Y. Hori, in *Modern Aspects of Electrochemistry* (Eds.: C. Vayenas, R. Whyte, M. Gamboa-Aldeco), Springer, New York, Vol. 42, **2008**, pp. 89–189.

[16] A. Kolodziej, P. Rodriguez, A. Cuesta, in *Electrochemical Reduction of Carbon Dioxide. Overcoming the Limitations of Photosynthesys. RSC Energy & Environment Series* (Eds.: F. Marken, D. Fermin), Royal Society Of Chemistry, Vol. 21, **2018**, pp. 88–110.

[17] A. J. Martín, G. O. Larrazábal, J. Pérez-Ramírez, *Green Chem.* **2015**, *17*, 5114–5130.

[18] J. F. Xie, Y. X. Huang, W. W. Li, X. N. Song, L. Xiong, H. Q. Yu, *Electrochim. Acta* **2014**, *139*, 137-144.

[19] R. Kas, R. Kortlever, H. Yilmaz, M. T. M. Koper, G. Mul, *ChemElectroChem* **2015**, *2*, 354-358.

[20] C. W. Li, J. Ciston, M. W. Kanan, *Nature* **2014**, *508*, 504–507.

[21] R. Kortlever, J. Shen, K. J. P. Schouten, F. Calle-Vallejo, M. T. M. Koper, *J. Phys. Chem. Lett.* **2015**, *6*, 4073–4082.

[22] F. Li, D. R. MacFarlane, J. Zhang, *Nanoscale* **2018**, *10*, 6235–6260.

[23] S. Gao, Y. Lin, X. Jiao, Y. Sun, Q. Luo, W. Zhang, D. Li, J. Yang, Y. Xie, *Nature* **2016**, *529*, 68–71.

[24] K. J. P. Schouten, F. Calle-Vallejo, M. T. M. Koper, *Angew. Chemie Int. Ed.* **2014**, *53*, 10858–10860.

[25] S. Verma, B. Kim, H.-R. Jhong, S. Ma, P. J. A. Kenis, *ChemSusChem* **2016**, *9*, 1972–1979.

[26] D. Pletcher, *Electrochem. Commun.* **2015**, *61*, 97–101.

[27] J. Ryczkowski, *Catal. Today* **2001**, *68*, 263–381.

[28] G. E. Ewing, *J. Chem. Phys.* **1962**, *37*, 2250–2256.

[29] R. P. Eischens, W. A. Pliskin, S. A. Francis, *J. Chem. Phys.* **1954**, *22*, 1786–1787.

[30] A. H. Reed, E. Yeager, *Electrochim. Acta* **1970**, *15*, 1345–1354.

[31] A. Bewick, K. Kunimatsu, B. Stanley Pons, *Electrochim. Acta* **1980**, *25*, 465–468.

[32] M. Osawa, M. Ikeda, *J. Phys. Chem.* **1991**, *95*, 9914–9919.

[33] M. Osawa, K. Ataka, K. Yoshii, T. Yotsuyanagi, *J. Electron Spectros. Relat. Phenomena* **1993**, *64–65*, 371–379.

[34] M. Osawa, K.-I. Ataka, K. Yoshii, Y. Nishikawa, *Appl. Spectrosc.* **1993**, *47*, 1497–1502.

[35] M. Osawa, *Bull. Chem. Soc. Jpn.* **1997**, *70*, 2861–2880.

[36] A. Cuesta, in *Vibrational Spectroscopy of Electrified Interfaces* (Eds.: A. Wieckowski, C. Korzeniewski, B. Braunschweig), John Wiley & Sons, Inc., Hoboken, NJ, USA, **2013**, pp. 266–306.

[37] J. E. Pander III, D. Ren, B. S. Yeo, *Catal. Sci. Technol.* **2017**, *7*, 5820–5832.

[38] B. L. Mojet, S. D. Ebbesen, L. Lefferts, *Chem. Soc. Rev.* **2010**, *39*, 4643.

[39] V. P. Tolstoy, I. V. Chernyshova, V. A. Skryshevsky, *Handbook of Infrared Spectroscopy of Ultrathin Films*, John Wiley & Sons, Inc., Hoboken, NJ, USA, **2003**.

[40] D. M. Kolb, in *Spectroelectrochemistry* (Ed.: R.J. Gale), Springer US, Boston, MA, **1988**, pp. 87–188.

[41] S. D. Barret, C. Lucas, R. Raval, in *Surface and Interface Science. Concepts and Methods* (Ed.: K. Wandelt), Wiley-VCH Verlag GmbH & Co. KGaA, Weinheim, Germany, Vol. 1, **2012**, pp. 311–374.

[42] C. Pecharromán, A. Cuesta, C. Gutiérrez, *J. Electroanal. Chem.* **2002**, *529*, 145–154.

[43] C. Pecharromán, A. Cuesta, C. Gutiérrez, *J. Electroanal. Chem.* **2004**, *563*, 91–109.

[44] P. A. Christensen, A. Hamnett, *Compr. Chem. Kinet.* **1989**, *29*, 1–77.

[45] A. Cuesta, G. Cabello, C. Gutiérrez, M. Osawa, *Phys. Chem. Chem. Phys.* **2011**, *13*, 20091–5.

[46] A. Cuesta, G. Cabello, M. Osawa, C. Gutiérrez, *ACS Catal.* **2012**, *2*, 728–738.

[47] A. Cuesta, G. Cabello, F. W. Hartl, M. Escudero-Escribano, C. Vaz-Domínguez, L. A. Kibler, M. Osawa, C. Gutiérrez, *Catal. Today* **2013**, *202*, 79–86.

[48] O. Ayemoba, A. Cuesta, *ACS Appl. Mater. Interfaces* **2017**, *9*, 27377–27382.

[49] H. Wang, Y.-W. Zhou, W.-B. Cai, *Curr. Opin. Electrochem.* **2017**, *1*, 73–79.

[50] P. R. Griffiths, in *Spectroscocpic Properties of Inorganic and Organometallic Compdounds: Techniques, Materials and Applications* (Eds.: J. Jarwood, R. Douthwaite, S. Duckett), Royal Society Of Chemistry, Vol. 44, **2013**, pp. 95–122.

[51] R. Aroca, in *Surface-Enhanced Vibrational Spectroscopy*, John Wiley & Sons, Ltd, Chichester, UK, **2007**, pp. 185–222.

[52] Z.-Q. Tian, B. Ren, D.-Y. Wu, *J. Phys. Chem. B* **2002**, *106*, 9463–9483.

[53] O. Krauth, G. Fahsold, A. Lehmann, *Surf. Sci.* **1999**, *433–435*, 79–82.

[54] S.-J. Huo, J.-Y. Wang, J.-L. Yao, W.-B. Cai, *Anal. Chem.* **2010**, *82*, 5117–5124.

[55] A. E. Bjerke, P. R. Griffiths, W. Theiss, *Anal. Chem.* **1999**, *71*, 1967–1974.

[56] A. Miki, S. Ye, M. Osawa, *Chem. Commun.* **2002**, 1500–1501.

[57] J.-Y. Wang, H.-X. Zhang, K. Jiang, W.-B. Cai, *J. Am. Chem. Soc.* **2011**, *133*, 14876–14879.

[58] Q.-X. Li, X.-K. Xue, Q.-J. Xu, W.-B. Cai, *Appl. Spectrosc.* **2007**, *61*, 1328–1333.

[59] H. Miyake, T. Okada, G. Samjeske, M. Osawa, *Phys. Chem. Chem. Phys.* **2008**, *10*, 3662–3669.

[60] H. Miyake, E. Hosono, M. Osawa, T. Okada, *Chem. Phys. Lett.* **2006**, *428*, 451–456.

[61] M. S. Anderson, *Appl. Phys. Lett.* **2003**, *83*, 2964–2966.

[62] R. F. Aroca, D. J. Ross, C. Domingo, *Appl. Spectrosc.* **2004**, *58*, 324A-338A.

[63] M. Osawa, in *Near-field Optics and Surface Plasmon Polaritons* (Ed.: S. Kawata), Springer Berlin Heidelberg, Berlin, Heidelberg, **2001**, pp. 163–187.

[64] G. Vasan, Y. Chen, A. Erbe, *J. Phys. Chem. C* **2011**, *115*, 3025–

3033.

[65] W. L. Barnes, A. Dereux, T. W. Ebbesen, *Nature* **2003**, *424*, 824–830.

[66] K. A. Willets, R. P. Van Duyne, *Annu. Rev. Phys. Chem.* **2007**, *58*, 267–297.

[67] K. M. Mayer, J. H. Hafner, *Chem. Rev.* **2011**, *111*, 3828–3857.

[68] M. Rycenga, C. M. Cobley, J. Zeng, W. Li, C. H. Moran, Q. Zhang, D. Qin, Y. Xia, *Chem. Rev.* **2011**, *111*, 3669–3712.

[69] W.-J. Bao, Z.-D. Yan, M. Wang, Y. Zhao, J. Li, K. Wang, X.-H. Xia, Z.-L. Wang, *Chem. Commun.* **2014**, *50*, 7787.

[70] I. Romero, J. Aizpurua, G. W. Bryant, F. J. García De Abajo, *Opt. Express* **2006**, *14*, 9988.

[71] U. K. Chettiar, P. Nyga, M. D. Thoreson, A. V. Kildishev, V. P. Drachev, V. M. Shalaev, *Appl. Phys. B* **2010**, *100*, 159–168.

[72] S. K. Ghosh, T. Pal, *Chem. Rev.* **2007**, *107*, 4797–4862.

[73] K. Lance Kelly, Eduardo Coronado, A. Lin Lin Zhao, G. C. Schatz*, *J. Phys. Chem. B* **2003**, *107*, 668–677.

[74] Y. Nishikawa, K. Fujiwara, K. Ataka, M. Osawa, *Anal. Chem.* **1993**, *65*, 556–562.

[75] D. A. Heaps, P. R. Griffiths, *Vib. Spectrosc.* **2006**, *42*, 45–50.

[76] Y. Yagil, P. Gadenne, C. Julien, G. Deutscher, *Phys. Rev. B* **1992**, *46*, 2503–2511.

[77] Z.-F. Su, S.-G. Sun, C.-X. Wu, Z.-P. Cai, *J. Chem. Phys.* **2008**, *129*, 044707.

[78] M. Osawa, in *Advances in Electrochemical Science and Engineering: Diffraction and Spectroscopic Methods in Electrochemistry* (Eds.: R.C. Alkire, D.M. Kolb, J. Lipkowsky, P.N. Ross), John Wiley & Sons, Ltd, Weinheim, Germany, Vol. 9, **2008**, pp. 269–314.

[79] H. Ghosh, T. Bürgi, *J. Phys. Chem. C* **2017**, *121*, 2355–2363.

[80] Z. Zhu, T. Zhu, Z. Liu, *Nanotechnology* **2004**, *15*, 357–364.

[81] Y. Nishikawa, T. Nagasawa, K. Fujiwara, M. Osawa, *Vib. Spectrosc.* **1993**, *6*, 43–53.

[82] D. Enders, T. Nagao, A. Pucci, T. Nakayama, M. Aono, *Phys. Chem. Chem. Phys.* **2011**, *13*, 4935.

[83] S. A. Maier, *Plasmonics: Fundamentals and Applications*, Springer US, New York, NY, **2007**.

[84] F. Le, D. W. Brandl, Y. A. Urzhumov, H. Wang, J. Kundu, N. J. Halas, J. Aizpurua, P. Nordlander, *ACS Nano* **2008**, *2*, 707–718.

[85] A. V Ermushev, B. V Mchedlishvili, V. A. Oleĭnikov, A. V Petukhov, *Quantum Electron.* **1993**, *23*, 435–440.

[86] R. Stanley, *Nat. Photonics* **2012**, *6*, 409–411.

[87] F. Neubrech, A. Pucci, T. W. Cornelius, S. Karim, A. García-Etxarri, J. Aizpurua, *Phys. Rev. Lett.* **2008**, *101*, 157403.

[88] R. Adato, A. A. Yanik, J. J. Amsden, D. L. Kaplan, F. G. Omenetto, M. K. Hong, S. Erramilli, H. Altug, *Proc. Natl. Acad. Sci.* **2009**, *106*, 19227–32.

[89] N. J. Halas, S. Lal, W.-S. Chang, S. Link, P. Nordlander, *Chem. Rev.* **2011**, *111*, 3913–3961.

[90] C. Huck, F. Neubrech, J. Vogt, A. Toma, D. Gerbert, J. Katzmann, T. Härtling, A. Pucci, *ACS Nano* **2014**, *8*, 4908–4914.

[91] O. Skibbe, M. Binder, A. Otto, A. Pucci, *J. Chem. Phys.* **2008**, *128*, 194703.

[92] G. T. Merklin, P. R. Griffiths, *Langmuir* **1997**, *13*, 6159–6163.

[93] S. Ye, L. Fang, Y. Lu, *Phys. Chem. Chem. Phys.* **2009**, *11*, 2480.

[94] O. Krauth, G. Fahsold, N. Magg, A. Pucci, *J. Chem. Phys.* **2000**, *113*, 6330.

[95] M. Heinen, Y. X. Chen, Z. Jusys, R. J. Behm, *Electrochim. Acta* **2007**, *53*, 1279–1289.

[96] E. M. Purcell, D. J. Morin, *Electricity and Magnetism*, Cambridge University Press, Cambridge, UK, **2013**.

[97] H. . Pearce, N. Sheppard, *Surf. Sci.* **1976**, *59*, 205–217.

[98] R. M. Hammaker, S. A. Francis, R. P. Eischens, *Spectrochim. Acta* **1965**, *21*, 1295–1309.

[99] E. Borguet, H.-L. Dai, *J. Chem. Phys.* **1994**, *101*, 9080–9095.

[100] I. Villegas, M. J. Weaver, *J. Chem. Phys.* **1994**, *101*, 1648–1660.

[101] G.-Q. Lu, S.-G. Sun, S.-P. Chen, L.-R. Cai, *J. Electroanal. Chem.* **1997**, *421*, 19–23.

[102] M. D. Porter, T. B. Bright, D. L. Allara, T. Kuwana, *Anal. Chem.* **1986**, *58*, 2461–2465.

[103] J. A. Mielczarski, R. H. Yoon, *J. Phys. Chem.* **1989**, *93*, 2034–2038.

[104] J. A. Mielczarski, *J. Phys. Chem.* **1993**, *97*, 2649–2663.

[105] J. A. Mielczarski, E. Mielczarski, J. Zachwieja, J. M. Cases, *Langmuir* **1995**, *11*, 2787–2799.

[106] P. A. Christensen, A. Hamnett, J. Munk, G. L. Troughton, *J. Electroanal. Chem.* **1994**, *370*, 251–258.

[107] R. Ortiz, A. Cuesta, O. P. Márquez, J. Márquez, J. A. Méndez, C. Gutiérrez, *J. Electroanal. Chem.* **1999**, *465*, 234–238.

[108] C.-X. Wu, H. Lin, Y.-J. Chen, W.-X. Li, S.-G. Sun, *J. Chem. Phys.* **2004**, *121*, 1553–1556.

[109] D. A. G. Bruggeman, *Ann. Phys.* **1935**, *416*, 636–664.

[110] D. Lotti, P. Hamm, J. P. Kraack, *J. Phys. Chem. C* **2016**, *120*, 2883–2892.

[111] J. P. Kraack, P. Hamm, *Chem. Rev.* **2017**, *117*, 10623–10664.

[112] F. Maroun, F. Ozanam, J.-N. Chazalviel, *J. Phys. Chem. B* **1999**, *103*, 5280–5288.

[113] H.-F. Wang, Y.-G. Yan, S.-J. Huo, W.-B. Cai, Q.-J. Xu, M. Osawa, *Electrochim. Acta* **2007**, *52*, 5950–5957.

[114] J. M. Delgado, J. M. Orts, A. Rodes, *Electrochim. Acta* **2007**, *52*, 4605–4613.

[115] H. Miyake, M. Osawa, *Chem. Lett.* **2004**, *33*, 278–279.

[116] E. Karabudak, E. Yüce, S. Schlautmann, O. Hansen, G. Mul, H. J. G. E. Gardeniers, *Phys. Chem. Chem. Phys.* **2012**, *14*, 10882.

[117] C. Vigano, J.-M. Ruysschaert, E. Goormaghtigh, *Talanta* **2005**, *65*, 1132–1142.

[118] E. Karabudak, R. Kas, W. Ogieglo, D. Rafieian, S. Schlautmann, R. G. H. Lammertink, H. J. G. E. Gardeniers, G. Mul, *Anal. Chem.* **2013**, *85*, 33–38.

[119] A. J. Bard, M. Stratmann, P. R. Unwin, Eds. , *Instrumentation and Electroanalytical Chemsitry*, Wiley-VCH, Weinheim, Germany, **2003**.

[120] J. Solla-Gullón, A. Aldaz, J. Clavilier, *Electrochim. Acta* **2013**, *87*, 669–675.

[121] M. Dunwell, Q. Lu, J. M. Heyes, J. Rosen, J. G. Chen, Y. Yan, F. Jiao, B. Xu, *J. Am. Chem. Soc.* **2017**, *139*, 3774–3783.

[122] P. Lobaccaro, M. R. Singh, E. L. Clark, Y. Kwon, A. T. Bell, J. W. Ager, *Phys. Chem. Chem. Phys.* **2016**, *18*, 26777–26785.

[123] T. Hatsukade, K. P. Kuhl, E. R. Cave, D. N. Abram, T. F. Jaramillo, *Phys. Chem. Chem. Phys.* **2014**, *16*, 13814–13819.

[124] C. W. Machan, M. D. Sampson, S. A. Chabolla, T. Dang, C. P. Kubiak, *Organometallics* **2014**, *33*, 4550–4559.
[125] A. A. Peterson, J. K. Nørskov, *J. Phys. Chem. Lett.* **2012**, *3*, 251–258.
[126] K. J. P. Schouten, E. Pérez Gallent, M. T. M. Koper, *J. Electroanal. Chem.* **2014**, *716*, 53–57.
[127] K. J. P. Schouten, Z. Qin, E. Pérez Gallent, M. T. M. Koper, *J. Am. Chem. Soc.* **2012**, *134*, 9864–9867.
[128] K. J. P. Schouten, E. Pérez Gallent, M. T. M. Koper, *J. Electroanal. Chem.* **2014**, *716*, 53–57.
[129] K. J. P. Schouten, E. Pérez Gallent, M. T. M. Koper, *ACS Catal.* **2013**, *3*, 1292–1295.
[130] K. P. Kuhl, E. R. Cave, D. N. Abram, T. F. Jaramillo, *Energy Environ. Sci.* **2012**, *5*, 7050–7059.
[131] A. Klinkova, P. De Luna, C.-T. Dinh, O. Voznyy, E. M. Larin, E. Kumacheva, E. H. Sargent, *ACS Catal.* **2016**, *6*, 8115–8120.
[132] Y. Li, S. H. Chan, Q. Sun, *Nanoscale* **2015**, *7*, 8663–8683.
[133] A. Wuttig, M. Yaguchi, K. Motobayashi, M. Osawa, Y. Surendranath, *Proc. Natl. Acad. Sci.* **2016**, *113*, E4585–E4593.
[134] J. L. Val, *J. Mol. Spectrosc.* **1971**, *40*, 367–371.
[135] N. J. Firet, W. A. Smith, *ACS Catal.* **2017**, *7*, 606–612.
[136] S. Zhu, B. Jiang, W.-B. Cai, M. Shao, *J. Am. Chem. Soc.* **2017**, *139*, 15664–15667.
[137] B. Beden, C. Lamy, A. Bewick, K. Kunimatsu, *J. Electroanal. Chem.* **1981**, *121*, 343–347.
[138] A. Bewick, *J. Electroanal. Chem. Interfacial Electrochem.* **1983**, *150*, 481–493.
[139] Z. Jusys, R. J. Behm, *Beilstein J. Nanotechnol.* **2014**, *5*, 747–759.
[140] A. Rodes, E. Pastor, T. Iwasita, *J. Electroanal. Chem.* **1994**, *369*, 183–191.
[141] A. Berná, A. Rodes, J. M. Feliu, F. Illas, A. Gil, A. Clotet, J. M. Ricart, *J. Phys. Chem. B* **2004**, *108*, 17928–17939.
[142] N. Gupta, M. Gattrell, B. MacDougall, *J. Appl. Electrochem.* **2006**, *36*, 161–172.
[143] A. Murata, Y. Hori, *Bull. Chem. Soc. Jpn.* **1991**, *64*, 123–127.
[144] G. Z. Kyriacou, A. K. Anagnostopoulos, *J. Appl. Electrochem.* **1993**, *23*, 483–486.
[145] M. R. Thorson, K. I. Siil, P. J. A. Kenis, *J. Electrochem. Soc.* **2013**, *160*, F69–F74.
[146] M. R. Singh, Y. Kwon, Y. Lum, J. W. Ager, A. T. Bell, *J. Am. Chem. Soc.* **2016**, *138*, 13006–13012.
[147] M. Dunwell, X. Yang, B. P. Setzler, J. Anibal, Y. Yan, B. Xu, *ACS Catal.* **2018**, *8*, 3999–4008.
[148] R. Kortlever, K. H. Tan, Y. Kwon, M. T. M. Koper, *J. Solid State Electrochem.* **2013**, *17*, 1843–1849.
[149] N. Sreekanth, K. L. Phani, *Chem. Commun.* **2014**, *50*, 11143–11146.
[150] D. Gao, H. Zhou, F. Cai, J. Wang, G. Wang, X. Bao, *ACS Catal.* **2018**, *8*, 1510–1519.
[151] M. F. Baruch, J. E. Pander, J. L. White, A. B. Bocarsly, *ACS Catal.* **2015**, *5*, 3148–3156.
[152] H. Hashiba, H. K. Sato, S. Yotsuhashi, K. Fujii, M. Sugiyama, Y. Nakano, *Sustain. Energy Fuels* **2017**, *1*, 1734–1739.
[153] J. D. Goodpaster, A. T. Bell, M. Head-Gordon, *J. Phys. Chem. Lett.* **2016**, *7*, 1471–1477.
[154] C. M. Gunathunge, X. Li, J. Li, R. P. Hicks, V. J. Ovalle, M. M. Waegele, *J. Phys. Chem. C* **2017**, *121*, 12337–12344.
[155] Y. Hori, O. Koga, Y. Watanabe, T. Matsuo, *Electrochim. Acta* **1998**, *44*, 1389–1395.
[156] Y.-G. Kim, J. H. Baricuatro, A. Javier, J. M. Gregoire, M. P. Soriaga, *Langmuir* **2014**, *30*, 15053–15056.
[157] J. H. Baricuatro, Y.-G. Kim, C. L. Korzeniewski, M. P. Soriaga, *Electrochem. Commun.* **2018**, *91*, 1–4.
[158] Y.-G. Kim, J. H. Baricuatro, M. P. Soriaga, *Electrocatalysis* **2018**, *9*, 526–530.
[159] Y.-G. Kim, A. Javier, J. H. Baricuatro, M. P. Soriaga, *Electrocatalysis* **2016**, *7*, 391–399.
[160] S. Lee, J. Lee, *ChemElectroChem* **2018**, *5*, 558–564.
[161] A. Wuttig, C. Liu, Q. Peng, M. Yaguchi, C. H. Hendon, K. Motobayashi, S. Ye, M. Osawa, Y. Surendranath, *ACS Cent. Sci.* **2016**, *2*, 522–528.
[162] X. Feng, K. Jiang, S. Fan, M. W. Kanan, *ACS Cent. Sci.* **2016**, *2*, 169–174.
[163] M. Gattrell, N. Gupta, A. Co, *J. Electroanal. Chem*. **2006**, *594*, 1–19.
[164] K. J. P. Schouten, Y. Kwon, C. J. M. van der Ham, Z. Qin, M. T. M. Koper, *Chem. Sci.* **2011**, *2*, 1902.
[165] E. Pérez-Gallent, M. C. Figueiredo, F. Calle-Vallejo, M. T. M. Koper, *Angew. Chemie Int. Ed.* **2017**, *56*, 3621–3624.
[166] E. Pérez-Gallent, G. Marcandalli, M. C. Figueiredo, F. Calle-Vallejo, M. T. M. Koper, *J. Am. Chem. Soc.* **2017**, *139*, 16412–16419.
[167] C. M. Gunathunge, V. J. Ovalle, M. M. Waegele, *Phys. Chem. Chem. Phys.* **2017**, *19*, 30166–30172.
[168] M. C. Figueiredo, I. Ledezma-Yanez, M. T. M. Koper, *ACS Catal.* **2016**, *6*, 2382–2392.
[169] A. V. Rudnev, U. E. Zhumaev, A. Kuzume, S. Vesztergom, J. Furrer, P. Broekmann, T. Wandlowski, *Electrochim. Acta* **2016**, *189*, 38–44.
[170] M. Papasizza, A. Cuesta, *ACS Catal.* **2018**, *8*, 6345–6352.
[171] T. A. Morhart, B. Unni, M. J. Lardner, I. J. Burgess, *Anal. Chem.* **2017**, *89*, 11818–11824.
[172] D. Perez-Guaita, K. M. Marzec, A. Hudson, C. Evans, T. Chernenko, C. Matthäus, M. Miljkovic, M. Diem, P. Heraud, J. S. Richards, et al., *Chem. Rev.* **2018**, *118*, 5330–5358.
[173] F. Neubrech, C. Huck, K. Weber, A. Pucci, H. Giessen, *Chem. Rev.* **2017**, *117*, 5110–5145.
[174] R. Adato, H. Altug, *Nat. Commun.* **2013**, *4*, 2154.
[175] C. Huck, J. Vogt, M. Sendner, D. Hengstler, F. Neubrech, A. Pucci, *ACS Photonics* **2015**, *2*, 1489–1497.

Text for Table of Contents

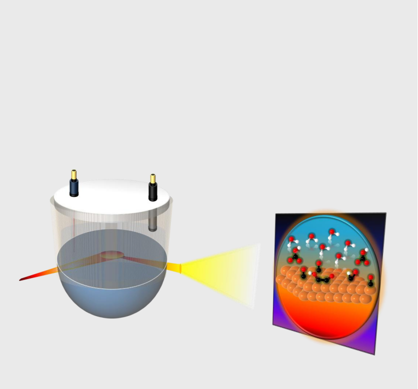

*Author(s), Corresponding Author(s)**

Page No. – Page No.

Title